

A Novel Survey for Young Substellar Objects with the *W*-band Filter. I. Filter Design and New Discoveries in Ophiuchus and Perseus

K. N. ALLERS^{1,2} AND MICHAEL. C. LIU³

¹*Department of Physics and Astronomy, Bucknell University, Lewisburg, PA 17837, USA*

²*Visiting Astronomer at the Infrared Telescope Facility, which is operated by the University of Hawaii under contract NNH14CK55B with the National Aeronautics and Space Administration.*

³*Institute for Astronomy, University of Hawai'i, 2680 Woodlawn Drive, Honolulu, HI 96822, USA*

ABSTRACT

We present the design and implementation of a medium-band near-IR filter tailored for detecting low-mass stars and brown dwarfs from the summit of Maunakea. The *W*-band filter is centered at 1.45 μm with a bandpass width of 6%, designed to measure the depth of the H₂O water absorption prominent in objects with spectral types of M6 and later. When combined with standard *J* and *H* photometry, the *W*-band filter is designed to determine spectral types to ≈ 1.4 subtypes for late-M and L dwarfs, largely independent of surface gravity and reddening. This filter's primary application is completing the census of young substellar objects in star-forming regions, using *W*-band selection to greatly reduce contamination by reddened background stars that impede broad-band imaging surveys. We deployed the filter on the UH 88 inch telescope to survey ~ 3 degree² of the NGC 1333, IC 348, and ρ Ophiuchus star-forming regions. Our spectroscopic followup of *W*-band selected candidates resulted in the confirmation of 48 ultracool dwarfs with a success rate of 89%, demonstrating the efficacy of this new filter and selection method.

1. INTRODUCTION

Broad-band filters in ground-based optical/infrared astronomy are designed to maximize sensitivity, with bandpasses placed in the regions of highest atmospheric transmission and spanning a large continuous swath of wavelengths (e.g. Bessell 2005). As a result, broad-band photometric systems have a small total number of filters (≈ 5), meaning multi-band images provide some basic spectral information on astronomical sources. It has long been appreciated that in addition to considering the Earth's atmosphere, consideration of the intrinsic spectrum of astrophysical sources during the design process can result in filters tailored for specific applications.

Such tailored filters typically sacrifice sensitivity and broad wavelength coverage in exchange for greater information content in the resulting photometry. Such filters are often used to detect rare classes of objects on the sky, where broad-band photometry does not sufficiently distinguish objects of interest from a much larger sea of undesired stars and galaxies. Well-known examples include the Strömgren filters for measuring temperature, surface gravity, and reddening of early-type stars (Strömgren 1966) and the methane-band filters for detection and spectral typing of T dwarfs (Rosenthal et al. 1996; Tinney et al. 2005). The young L dwarf companion G 196-3B was found by Rebolo et al. (1998) using narrow-band optical filters described by Martín et al. (1996).

Najita et al. (2000) pioneered the application of tailored filters for young low-mass stars and brown dwarfs. With spectral types of late-M and later (and thus commonly referred to as ultracool objects), these objects have ample water absorption in their photospheres, which is manifested in their spectra as deep, broad absorption troughs, analogous to the telluric bands that demarcate the traditional *JHK* broad-band filters. Najita et al. used a combination of 3 narrow-band ($\Delta\lambda/\lambda \approx 1\%$) filters in the Hubble Space Telescope (HST)/ NICMOS imager (F166N, F190N, and F215N) to measure the 1.9 μm water absorption for objects in the IC 348 star-forming region. The first and third filters are analogous to the *H* and *K* filters and measure the bright continuum flux, while the F190N filter resides in the water band. To derive spectral types for all sources in their images, they formed a reddening-independent *Q* index (Johnson & Morgan 1953), calibrated from IC 348 sources with spectral types previously measured spectroscopically. This resulted in a spectral-typing precision of ≈ 1 subtype for objects with water absorption. (This method cannot classify earlier-type sources, which lack water absorption, but can distinguish such objects from later-type ones.) They estimate reddenings for objects in their HST photometry from the two resulting colors (F166N-F190N and F190N-F215N). Their work resulted in a deep measurement of the initial mass function (IMF) in this cluster, as well as enabling the first robust survey for circumstellar disks at such low masses (Liu et al. 2003). A somewhat similar approach for ground-based and aircraft-based observations based on medium-band IR filters was developed by Mainzer & McLean 2003.

The shape and low-mass cutoff of the IMF are signatures of the star (and brown dwarf) formation process. Measuring these properties and their dependence on environment provides the empirical foundation for testing theoretical models. In recent years, wide-field optical and infrared imagers have pushed photometric surveys of star-forming regions ever deeper (e.g. Alves de Oliveira et al. 2010; Scholz et al. 2012) and thus to lower masses, down to $\approx 5 M_{\text{Jup}}$ (e.g. Lodieu et al. 2013; Zapatero Osorio et al. 2017). Using broad-band filters, such surveys readily identify hundreds of brown-dwarf candidates in young ($\sim \text{Myr}$) star-forming regions. The largest obstacle to this approach is its need for spectroscopic followup, since deeper imaging also means an increase in contaminating sources (mostly reddened background stars). Because spectroscopy of large samples is telescope-time intensive, strict photometric selection criteria are commonly used to reduce the number of contaminants in their samples. Such criteria may be problematic, by relying on evolutionary model isochrones that have not been validated at such young ages and low masses. Similarly, recent studies of $\sim 10\text{--}100$ Myr old field brown dwarfs find that objects can be fainter in the near-IR than expected (e.g. Liu et al. 2013; Faherty et al. 2016; Liu et al. 2016). So altogether, broad-band surveys may have undesirable and/or uncertain incompleteness in the low-mass regime. Relaxing the photometric selection criteria to increase completeness is not a practical solution, since the increased number of candidates further strains follow-up spectroscopy (Barsony et al. 2012).

As demonstrated by Najita et al. (2000), tailored filters are appealing for measuring the low-mass end of the IMF. We describe here the design, implementation, and characterization of a new near-IR filter tailored for selection of brown dwarfs using ground-based telescopes. Our approach maintains the efficiency of wide-field imaging, namely measuring the properties of many objects in a single pointing, while also providing spectral information. The results is a very high confirmation rate for spectroscopic followup. Section 2 provides the quantitative design of the filter, and Section 3 provides the performance analysis. Section 4 presents our initial use of this filter on the UH 88 inch telescope. Section 5 describes the photometric selection and spectroscopic followup, with Section 6 discussing

the confirmation rate of our survey. Finally, Section 7 gives our conclusions and discusses future directions.

2. DESIGN OF A CUSTOM NEAR-IR FILTER

We aimed to design a custom near-IR filter that photometrically selects brown dwarfs in star-forming regions. We employed the following criteria when considering possible filters:

1. In combination with broad-band photometry, our custom filter must be able to distinguish late-M and L dwarfs from background field stars *independent of interstellar reddening*. For the ages of star-forming regions and young clusters, the stellar/substellar boundary occurs at a spectral type of \sim M6 (e.g., Basri et al. 1996; Martín et al. 1998; Alves de Oliveira et al. 2010).
2. Our filter must lie in the wavelength range of 1.0–1.8 μ m, a limitation set by the wavelength range of ULBCam on the UH 88 inch telescope.
3. To maximize observing efficiency, the filter should have as wide a bandwidth as possible.

Of course, such a filter would also be suitable for selecting low-mass stars and brown dwarfs not in star-forming regions, where there is no extinction, though in this case traditional broad-band filters would generally offer superior performance.

2.1. Synthetic Photometry

To test the ability of various possible filter designs to discriminate between field stars and young brown dwarfs, we compiled a training sample of low-mass stars and brown dwarfs having high quality near-IR spectra. We used:

- Our own SpeX near-IR spectra of optically classified young brown dwarfs in nearby star-forming regions (ages of \sim 1–5 Myr) having spectral types ranging from M5 to M8 (Table 1).
- Published spectra of young objects in IC 348 and Taurus (ages of \sim 3 Myr) from Muench et al. (2007) and Allers et al. (2009).
- Published near-IR spectra of young M and L dwarfs with VL-G gravity classifications (estimated ages of \sim 10 Myr) from Allers & Liu (2013).
- Published M1–L9 dwarf spectral standards (expected to have typical solar neighborhood ages of a few Gyr) from Cushing et al. (2005) and Kirkpatrick et al. (2010).

For each object in our training sample, we calculated synthetic photometry for the J_{MKO} and H_{MKO} filters (Tokunaga et al. 2002). We then synthesized photometry for ideal (100% transmission) filters centered at wavelengths of $1.0 < \lambda_{\text{center}} < 1.8 \mu\text{m}$ (in central wavelength steps of 0.01 μm) and filter bandwidths equal to 2%, 4%, 6%, and 8% of the central wavelength. Thus, our design analysis considered 324 potential filters.

For each object, we calculated the flux through each filter as

$$\langle F_{\lambda,w} \rangle = \frac{\int \lambda F_{\lambda}(\lambda) S(\lambda) d\lambda}{\int \lambda S(\lambda) d\lambda} \quad (1)$$

Table 1. IRTF/SpEx Observing Log for Training Sample Brown Dwarfs in Star-Forming Regions

Object	SpT	Ref.	UT Date	Grat	Slit (")	R	sec z	$N_{\text{exp}} \times t$ (s)	T_{int} (s)	$\langle S/N \rangle (Y, J, H, K)$
2MASS J03441558+3209218	M7.5	L16	2001 Nov 6	ShortXD	0.5×15	1200	1.17	14×120.0	1680.0	18, 41, 43, 48
2MASS J03443103+3205460	M5.5	L16	2001 Nov 6	ShortXD	0.5×15	1200	1.13	8×120.0	960.0	43, 94, 103, 109
IfAHA 73	M7.25	L16	2001 Nov 6	ShortXD	0.5×15	1200	1.03	6×120.0	720.0	41, 90, 93, 112
2MASS J03443545+3208563	M5.25	L16	2001 Nov 6	ShortXD	0.5×15	1200	1.21	6×120.0	720.0	55, 123, 149, 168
2MASS J03443551+3208046	M5.25	L16	2001 Nov 7	LowRes15	0.5×15	120	1.19	6×120.0	720.0	189, 273, 216, 166
2MASS J03443595+3209243	M5.25	L16	2001 Nov 7	LowRes15	0.5×15	120	1.03	6×120.0	720.0	155, 254, 200, 138
2MASS J03443814+3210215	M6	L16	2001 Nov 6	ShortXD	0.5×15	1200	1.51	14×120.0	1680.0	49, 105, 94, 109
2MASS J03443886+3206364	M6	L16	2001 Nov 6	ShortXD	0.5×15	1200	1.07	6×120.0	720.0	51, 102, 105, 112
2MASS J03443920+3208136	M8	L16	2001 Nov 7	LowRes15	0.5×15	120	1.04	6×120.0	720.0	78, 150, 117, 86
2MASS J03443943+3210081	M5	L16	2001 Nov 6	ShortXD	0.5×15	1200	1.52	8×120.0	960.0	62, 109, 109, 112
[SS94] V410 X-ray 6	M5.5	B02	2002 Nov 25	ShortXD	0.5×15	1200	1.01	8×120.0	960.0	190, 256, 216, 195
[BHS98] MHO 5	M6	B02	2002 Nov 25	ShortXD	0.5×15	1200	1.07	7×120.0	840.0	115, 187, 163, 153
[BHS98] MHO 8	M6	B02	2002 Nov 25	ShortXD	0.5×15	1200	1.51	6×120.0	720.0	157, 289, 245, 173
[MDM2001] CFHT-BD-Tau 2	M7.5	B02	2001 Nov 6	ShortXD	0.5×15	1200	1.69	6×120.0	720.0	27, 75, 91, 116
GM Tau	M5	H14	2002 Nov 25	ShortXD	0.5×15	1200	1.71	6×120.0	720.0	33, 107, 102, 102
ISO-Oph 32	M8	W05	2004 Jul 5	ShortXD	0.5×15	1200	1.43	8×180.0	1440.0	135, 260, 204, 205
ISO-Oph 102	M5.5	W05	2004 Jul 5	ShortXD	0.5×15	1200	1.48	8×180.0	1440.0	150, 280, 263, 319

NOTE—The last column gives the median S/N of the spectrum within the standard IR bandpasses

References—B02: Briceño et al. (2002); H14: Herczeg, & Hillenbrand (2014); L16: Luhman et al. (2016); W05: Wilking et al. (2005)

$S(\lambda)$ is the total system response including the atmospheric transmission¹ and filter response. We did not include the throughput of the telescope and instrument nor the quantum efficiency of the detector, as our filter design could potentially be used in multiple near-IR imagers. Since we used photometric colors in subsequent analysis, we did not apply absolute flux calibrations to our synthetic photometry. To enable transformation between flux ratios and colors (in the Vega photometric system), we also computed synthetic photometry for the Vega spectrum of Bohlin (2007)² and assume zero color for Vega.

2.2. Reddening-independent Index

Since we intended to use our custom filter to find young brown dwarfs in star-forming regions, where interstellar extinction can be significant, we wanted to be able to distinguish candidate members from foreground and background field stars independent of reddening. Following a similar method as Najita et al. (2000), we defined a reddening-independent index

$$Q = J - W + e \times (H - W) \quad (2)$$

W refers to the magnitude of the object in our proposed filter, J and H are magnitudes in the standard broad-band filters, and e is the ratio of reddening color excesses

$$e = \frac{A_J - A_W}{A_W - A_H} \quad (3)$$

¹ We used the atmospheric absorption spectrum for Maunakea from the Gemini Observatory webpages (<http://www.gemini.edu/sciops/telescopes-and-sites/observing-condition-constraints/ir-transmission-spectra>) for an airmass of 1.5 and precipitable water vapor content of 1.6 mm.

² ftp://ftp.stsci.edu/cdbs/calspec/ascii/alpha_lyr_stis_005.ascii

For each filter (J, H and every potential custom filter), we calculated the selective extinction, A_λ , as follows: to represent the background population, first we reddened the spectrum of Gl 270 (Kirkpatrick et al. 2010) by $A_V=10$ mag using the $R_V=3.1$ reddening law of Fitzpatrick (1999). Next, we calculated the flux (Equation 1) through the filter for both the reddened and unreddened spectrum. We then calculated the selective extinction for each filter as:

$$A_\lambda = -2.5 \log \left(\frac{F_{\lambda,reddened}}{F_\lambda} \right) / A_V \quad (4)$$

Using the selective extinction values for J, H and a potential custom filter, we calculated e and determined Q , the reddening insensitive index of each object in our training sample for each of our 324 potential filters.

The near-IR spectra of M and L dwarfs contain a wealth of features that are sensitive to effective temperature and gravity (e.g. see Allers & Liu 2013, and references therein). Many of these features are alkali lines or molecular bandheads that are too narrow to be accurately quantified by a photometric filter. Our custom filter is thus most sensitive to differences in continuum variations, in particular the deep and broad H₂O and FeH absorption features that shape the J and H band continua of M and L dwarfs. These broad H₂O and FeH continuum features vary monotonically across the late-M and L spectral range (e.g. Cushing et al. 2005; Testi 2009) so the ability to cull contaminants from a photometric sample is tied to our custom filter’s sensitivity to spectral type.

We examined our custom filter’s sensitivity to spectral type for our training sample. Figure 1 shows examples of Q vs. SpT for three possible filters. To determine the best central wavelength for our filter, we calculated the scatter (σ_Q) of the Q values about a linear fit of Q vs. SpT for objects in our training sample with SpT later than M6. The uncertainty in SpT was determined as σ_Q divided by the slope of the linear fit ($dQ/d(SpT)$). Figure 2 shows the uncertainty in SpT (as a result of the scatter in Q) for filters with central wavelengths varying from 1.0 to 1.8 μm . Based on the low SpT scatter, we chose to center our filter at 1.45 μm .

Having narrowed down the central wavelength of our filter to $\lambda_{\text{center}}=1.45 \mu\text{m}$, we then determined the optimal filter bandwidth. Ideally, the filter bandwidth should be as wide as possible to reduce integration time, without sacrificing sensitivity to SpT. We tested filters of 2%, 4%, 6% and 8%, and found that the uncertainty and scatter in SpT changed by a negligible amount from 2% to 6% (Figure 2). Thus, we determined that the optimal custom filter for our purposes is a 6% wide filter centered at 1.45 μm .

3. PERFORMANCE ANALYSIS

Our filter was fabricated by Barr and Associates. Figures 3 and 4 show the transmission profile of a witness sample created at the same time as our filter and scanned while cooled to 50 K. We use this cold witness scan in subsequent analysis, but also conducted a warm scan of our filter and found negligible differences in the filter throughput. As shown in Figure 5, our filter easily separates ultracool dwarfs from field stars using only J, H , and W -band photometry, thanks to its sensitivity to deep H₂O absorption in the atmospheres of late-M and L dwarfs. Figure 6 shows the reddening-insensitive index Q (Equation 2) determined for our training sample as a function of spectral type. Based on the scatter about a linear fit to SpT versus Q for young M6–L5 type objects, our filter should be able to determine spectral type with a precision of 1.4 subtypes.

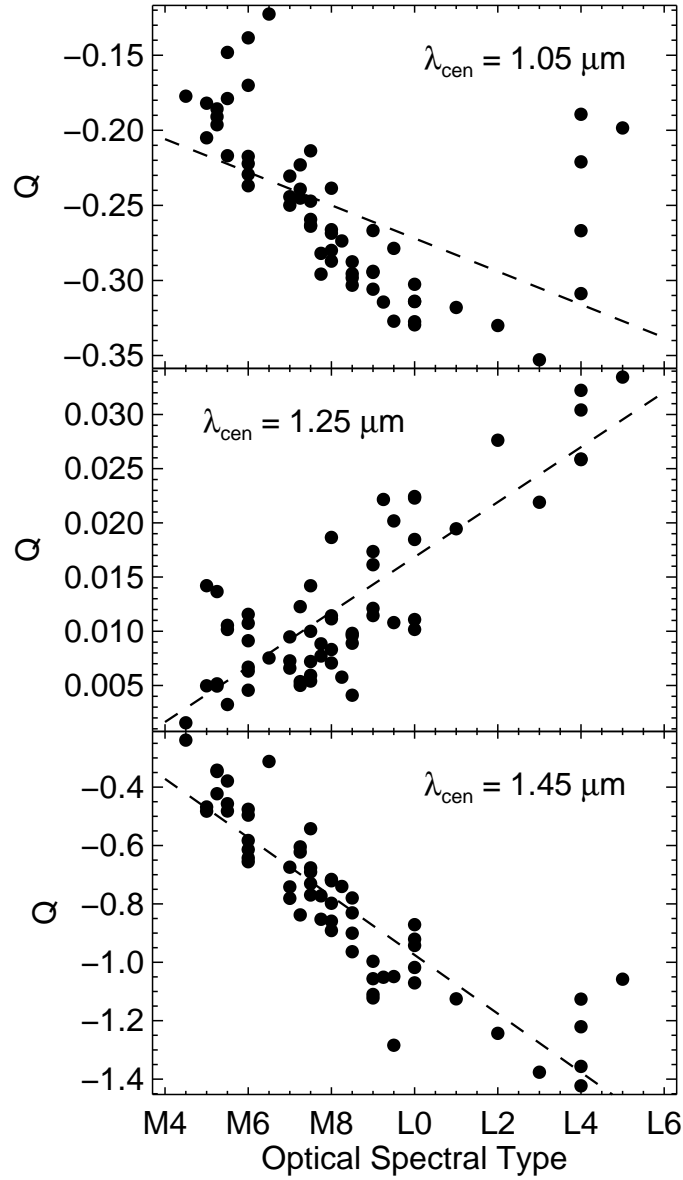


Figure 1. Reddening insensitive indices (Q) calculated from synthetic photometric (§2.1) of our training sample for three potential filters. Q values are calculated as described in §2.2 for filters with central wavelengths of 1.05 (top panel), 1.25 (middle panel), and 1.45 μm (bottom panel) and bandwidths equal to 6% of the central wavelength. Dashed lines show the results of a linear fit to Q vs. optical spectral type.

The majority of objects in our training sample have spectral types of M5–L5, for which Q shows a linear dependence on spectral type. Cooler T dwarfs also have significant H_2O absorption, but their methane-dominated spectra do not follow the same linear trend seen for M5–L5 objects, and the absorption at 1.45 μm is so deep that photometric sensitivity can be a limiting factor for detection.

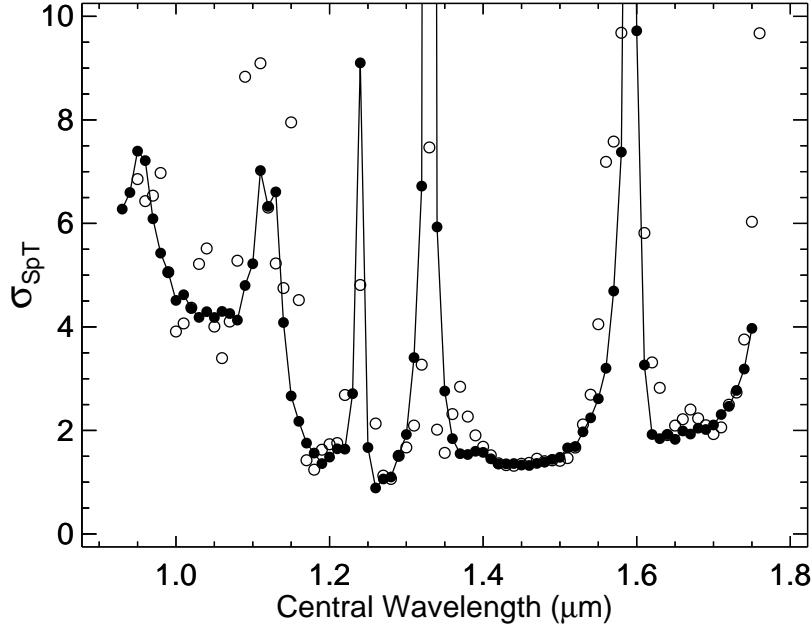


Figure 2. Spectral type uncertainty (in subtypes) vs. filter central wavelength. The spectral type uncertainty was determined from the scatter (σ_Q) about a linear fit of Q vs. SpT for each filter and divided by the slope of the fit. Solid circles (connected by a solid line) show σ_{SpT} for 6% wide filters. Open circles show σ_{SpT} for 2% wide filters. Based on this analysis, we decided to fabricate a 6% wide filter centered at $1.45 \mu\text{m}$.

Nonetheless, our custom filter can distinguish T dwarfs from background stars (Figure 7), though broad band and methane filters may be better suited to their detection and characterization.

3.1. *W* Filter Fluxes and Wavelengths for Vega

Using the spectrum of Bohlin (2007), we calculate the flux density (F_λ), isophotal wavelength (λ_{iso}), and effective wavelength (λ_{eff}) for Vega in the *W* filter. We first scale the Vega spectrum to $3.46 \times 10^{-9} \text{ W m}^{-2} \mu\text{m}^{-1}$ at a wavelength of $0.5556 \mu\text{m}$ (Megessier 1995). For our filter, we calculate a flux density of $1.79 \times 10^{-9} \text{ W m}^{-2} \mu\text{m}^{-1}$ and isophotal and effective wavelengths of $1.445 \mu\text{m}$ for Vega, using a system response that includes our filter profile and atmospheric transmission for 1.6 mm of precipitable water vapor and an airmass of 1.5. The *W*-band flux density of Vega in frequency units³ is $F_\nu = 1180 \text{ Jy}$. Using Equation 9 from Tokunaga & Vacca (2005), we calculate an AB magnitude of $W_{\text{AB}} = 1.25 \text{ mag}$ for Vega.

3.2. Comparison of Integration Times

³ Calculated as $\langle F_{\nu,W} \rangle = \frac{\int F_\nu(\nu)S(\nu)/\nu d\nu}{\int S(\nu)/\nu d\nu}$ from the Vega spectrum, scaled to have $F_\nu = 3630 \text{ Jy}$ in *V*-band.

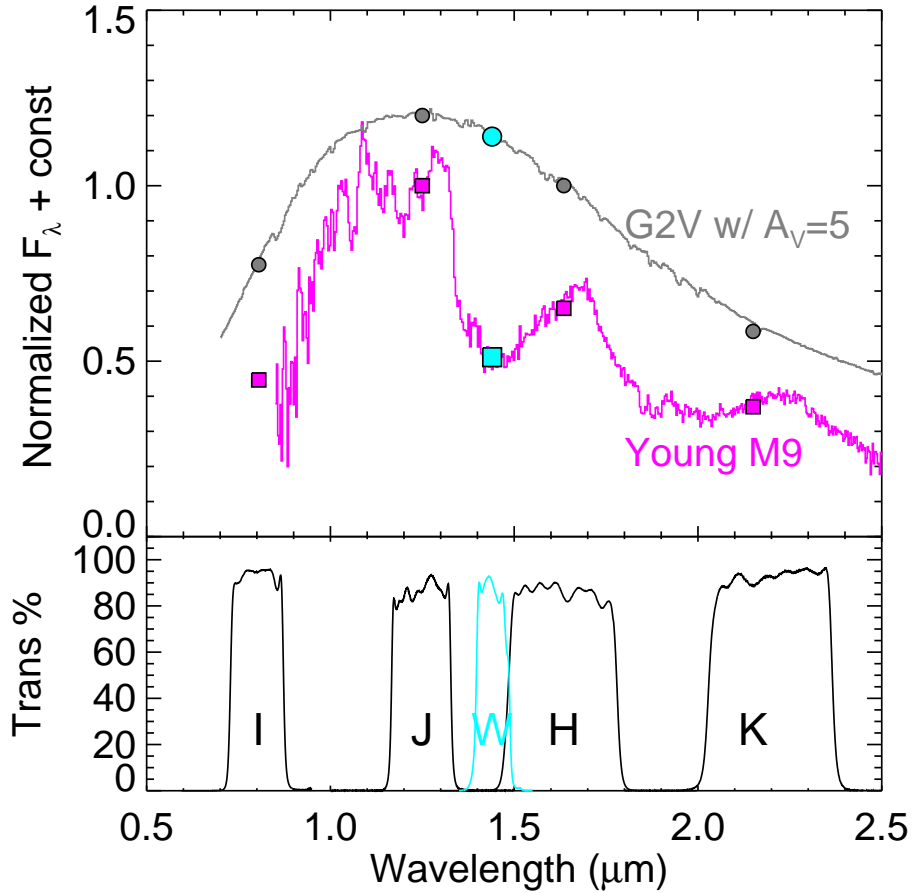


Figure 3. Top: spectra and photometry for a G2V star (HD 142093; Burgasser 2014) reddened by $A_V = 5$ mag and a young M9 (KPNO 12; Muench et al. 2007). The broad-band I, J, H, K colors of these two objects are nearly indistinguishable. Bottom: our custom W filter breaks the degeneracy in broad-band colors for these two objects due to deep H_2O absorption in the spectra of ultracool dwarfs at the transmission wavelengths of our filter.

To determine the necessary integration times for our custom filter, we computed the total flux from Vega that makes it onto the detector ($\int \lambda F_\lambda(\lambda) S(\lambda) d\lambda$), assuming that losses due to reflections and detector quantum efficiency are wavelength-independent and using a telluric transmission spectrum for 1.6 mm of precipitable water vapor at an airmass of 1.5. For Vega, the detected flux in the W -band is 0.26 times that in the H -band. The shorter wavelength and narrower bandwidth of the W filter compared to H , however, means that the W filter has 7.1 times lower sky background.⁴ We calculated the relative noise levels assuming that the photometric noise is dominated by Poisson noise of the sky background (i.e. neglecting readnoise and moonlight), and that the seeing is identical in W -band and H -band. We find that to reach the same Vega-magnitude with the same signal-to-

⁴ We calculated the sky background using the ATRAN models (Lord 1992) for a pwv of 1.6 mm and an airmass of 1.5. The sky background spectrum also includes the contribution of a 273 K blackbody as described on the Gemini webpages (<http://www.gemini.edu/sciops/telescopes-and-sites/observing-condition-constraints/ir-background-spectra>).

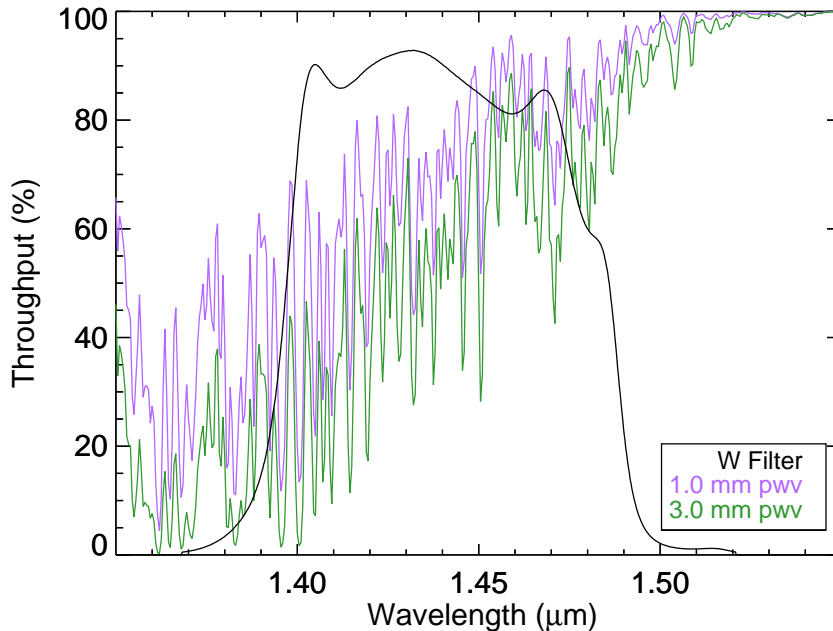


Figure 4. The throughput of our custom filter (black) compared to the sky transparency for precipitable water vapor contents of 1.0 and 3.0 mm and an airmass of 1.5. The telluric absorption spectra calculated using the ATRAN software (Lord 1992) calculated for the conditions on Maunakea and available for download on the Gemini Observatory webpages (<http://www.gemini.edu/sciops/telescopes-and-sites/observing-condition-constraints/ir-transmission-spectra>).

noise ratio (S/N), observations using the *W* filter require ≈ 2 times the integration time required for *H*-band. For young late-M and L type objects, the intrinsic *W*-band magnitude is fainter than in *H*-band (Figure 5), so even deeper *W*-band observations are needed to achieve the same S/N as *H*-band observations.

3.3. The Effects of Precipitable Water Vapor

The deep H₂O absorption features that allow our filter to identify M and L-type objects coincide with deep telluric absorption features. Thus, the throughput of the filter will depend on airmass and the atmospheric precipitable water vapor (pwv) content. Figure 4 shows the throughput of the *W* filter as well as telluric transmission for precipitable water vapor contents of 1.0 and 3.0 mm (at an airmass of 1.5) which correspond to the 20th and 80th percentile of conditions on Maunakea.⁵ The median precipitable water vapor for Maunakea is 1.6 mm, which is what we use in our determination of e (Equation 3). For the spectrum of Vega, a change in pwv from 1 mm to 3 mm results in a 26% reduction in total system response ($S(\lambda)$ in Equation 1). Similarly, under median pwv conditions (1.6 mm), a change in airmass from 1 to 2 results in a 17% reduction in total system response.

⁵ <http://www.gemini.edu/sciops/telescopes-and-sites/observing-condition-constraints/mk-water-vapour-statistics>

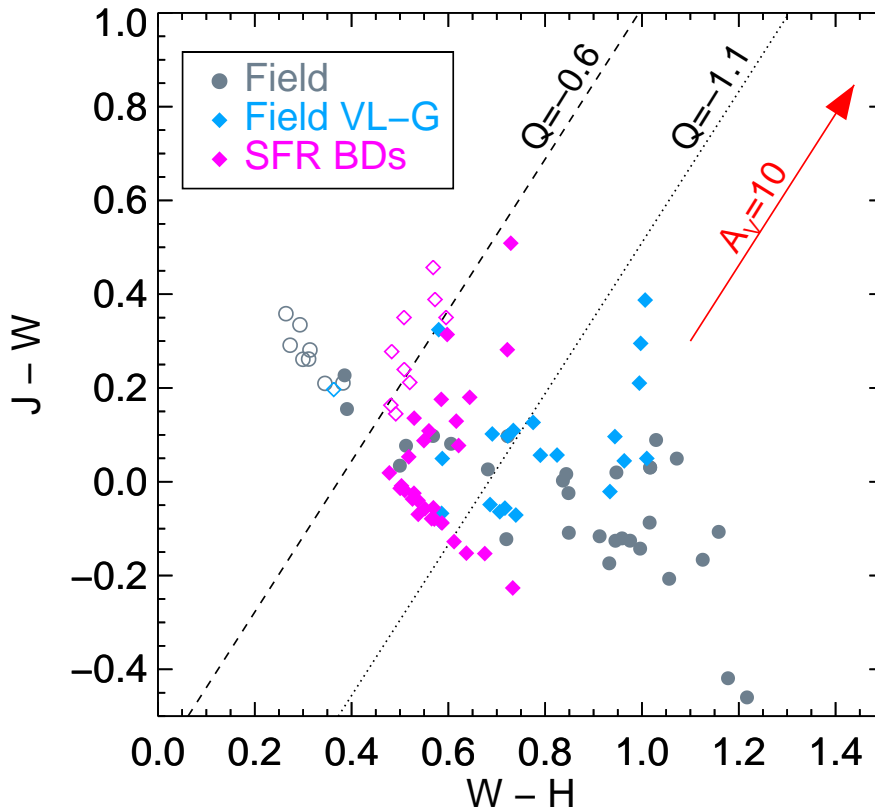


Figure 5. $W - H$ and $J - W$ colors synthesized for our training sample (§2.1). The gray circles are synthetic photometry of M1–T5 field dwarf spectral standards (Cushing et al. 2005; Kirkpatrick et al. 2010). The blue diamonds are young field brown dwarfs with gravity classifications of VL-G (Allers & Liu 2013). The magenta diamonds are young objects in the Taurus, IC 348, and Ophiuchus star-forming regions (Table 1; Muench et al. 2007; Allers et al. 2009). A reddening vector for $A_V = 10$ is shown. The dashed line denotes the colors of objects having a reddening-insensitive index of -0.6 and roughly indicates the substellar boundary for young objects. The dotted line denotes the colors of objects having a reddening-insensitive index of -1.1 , which corresponds to the M/L spectral type transition. Solid symbols indicate objects with spectral types of M6 and later. Open symbols indicate objects with spectral types earlier than M6.

Thus, changes in atmospheric pwv and airmass affect the zero-point of the W filter, so photometric calibration should not be done using non-contemporaneous photometric standard fields.

To see if pwv will affect our calculation of Q , we can look at the change in effective wavelength. For a pwv of 1 mm (at an airmass of 1.5), the effective wavelength of the W filter for Vega is $1.4436 \mu\text{m}$. For a pwv of 3 mm, the effective wavelength shifts very slightly redward, to $1.4470 \mu\text{m}$. The calculated flux density for Vega also has a very small change with pwv. A change in pwv from 1 to 3 mm changes Vega’s calculated flux density by only 0.8%. Thus, though precipitable water vapor

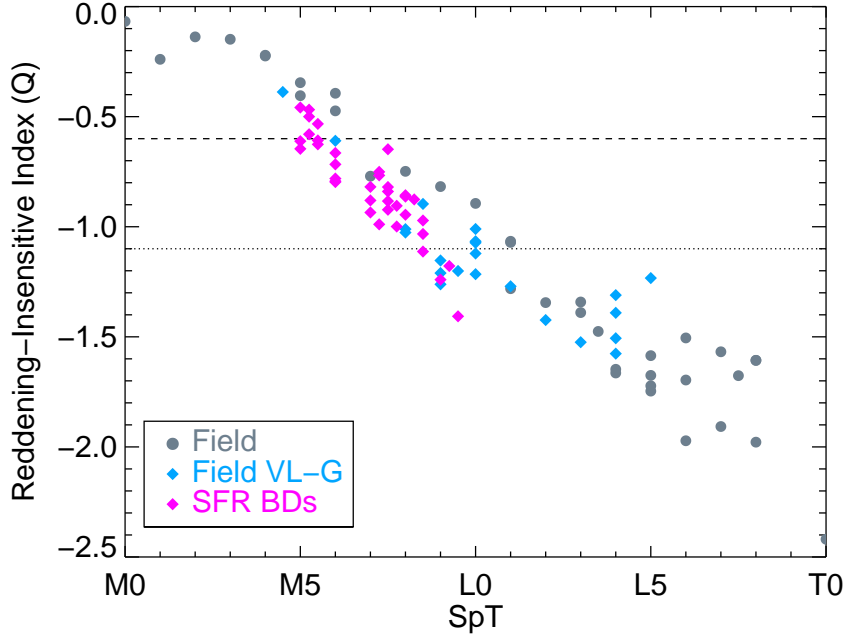


Figure 6. Relation between spectral type and the reddening-insensitive index, Q , calculated from synthesized J , H , and W -band photometry of our training sample (§2.1). The legend is the same as for Figure 5. The dashed line denotes $Q = -0.6$, below which the Q value indicates a spectral type later than M6, corresponding to the substellar boundary for young objects. The dotted line denotes $Q = -1.1$, corresponding to the M/L spectral type transition.

changes the throughput of the filter, if care is taken in photometric calibration (§4.2), pwv has a negligible effect on the photometric colors and calculated Q values.

3.4. Selective Extinction

The effects of interstellar extinction are wavelength-dependent. The selective extinction for a given filter, A_λ , is dependent on the wavelength of filter as well as the spectral shape of the light being attenuated by the dust. The selective extinction ratio, A_λ/A_V , thus depends on the interstellar reddening law (i.e. properties of the attenuating dust), the amount of extinction, and the spectral energy distribution of the object being attenuated (e.g. see Fiorucci & Munari 2003). We calculate the selective extinction for spectra of Vega (Bohlin 2007), an M0 (Gl207, Kirkpatrick et al. 2010) and a young L0 (the L0 VL-G standard, 2M2213-12 from Allers & Liu 2013). Using Equation 4, we calculate the selective extinctions A_J , A_H , and A_W using the reddening law of Fitzpatrick (1999) for $R_V=3.1$ and 5.0 and $A_V = 1, 5, 10,$ and 20 mag. We find that the values of selective extinction change very little. For example, at all values of A_V and R_V the value of A_W/A_V ranges only from 0.197 to 0.203 for all three spectra.

Though the values for selective extinction vary little, the values for e (Equation 3) have a much larger variation (1.46-1.93). Table 2 summarizes the variation in e with SpT, A_V , R_V , airmass, and

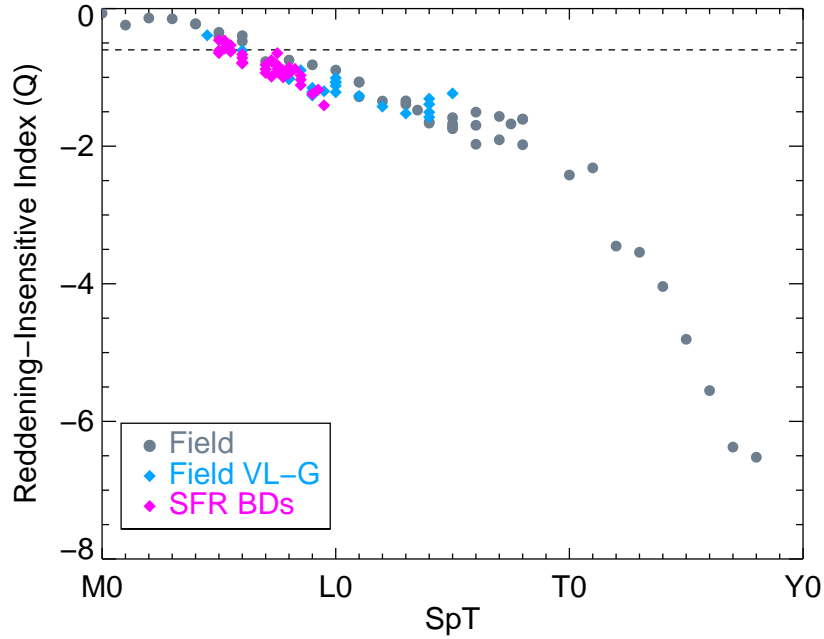


Figure 7. Same as Figure 6, but showing an extension to T dwarfs using spectral standards from Kirkpatrick et al. (2010).

Table 2. Selective Extinction (e) Ratios

SpT ^a	A_V	R_V	Airmass	pwv	e_{MKO}
	(mag)			(mm)	
M0	10.0	3.1	1.5	1.6	1.61^a
M0	10.0	5.0	1.5	1.6	1.74
M0	1.0	3.1	1.5	1.6	1.67
M0	20.0	3.1	1.5	1.6	1.55
M0	10.0	3.1	1.0	1.0	1.58
M0	10.0	3.1	2.0	3.0	1.67
A0	10.0	3.1	1.5	1.6	1.74
L0	10.0	3.1	1.5	1.6	1.56

^aThe value of e adopted for our data reduction and analysis.

pwv. Since the goal is to distinguish between background stars and ultracool dwarfs, choosing a value of e appropriate for the reddened background population ensures that fewer contaminants are selected by our filter. The median A_V for the regions of Perseus and Ophiuchus in our survey is

4 mag. However, the choice of e more strongly affects calculated Q values (Equation 2) for highly reddened objects. Thus, for calculating Q from W , J_{MKO} and H_{MKO} , we chose to adopt $e_{\text{MKO}} = 1.61$ the value calculated for an M0 star reddened by $A_V = 10$ mag and $R_V = 3.1$ and observed at an airmass of 1.5 and pwv content of 1.6. Because *Two Micron All Sky Survey* photometry is readily available, we also calculate $e_{2\text{MASS}} = 1.52$ using the 2MASS filter profiles, so that W filter photometry can also be combined with $J_{2\text{MASS}}$ and $H_{2\text{MASS}}$.

We tested how our choice of e would affect our selection of ultracool dwarf candidates by examining how our calculated Q value (Equation 2) and corresponding SpT (from the linear relation shown in Figure 6) for a young L0 are affected by variations in reddening and observing conditions. For moderate reddening ($A_V < 10$ mag), we find that our adoption of $e_{\text{MKO}} = 1.61$ leads to variations in the determined spectral type of a reddened young L0 of < 0.5 subtypes, well below the scatter in the SpT versus Q relation in Figure 6.

Our choice of e can cause reddened background stars to have artificially lower Q values. For background objects with spectral types of M0, moderate reddening ($A_V < 10$ mag) causes a negligible change in calculated Q values, as expected for a reddening-insensitive index. For highly reddened objects, however, Q has some sensitivity to extinction. If reddened by $A_V = 30$ mag, an M0 star has a calculated Q value that is 0.2 lower than its Q for moderate extinctions. This indicates that care should be taken when applying Q selection criteria to highly reddened objects.

4. OBSERVATIONS AND DATA REDUCTION

We conducted a pilot survey by imaging two star-forming molecular clouds in broad-band J and H filters, as well as our custom W filter. We chose to image the Ophiuchus and Perseus star-forming regions, as they are relatively nearby (~ 140 pc and ~ 300 pc, respectively), which allowed us to efficiently verify candidates spectroscopically (§5). In Ophiuchus, our survey covered ~ 1.6 square degrees and included the L1688 and L1689 regions, as well as a region to the west of L1688 surveyed in Allers et al. (2006). The ages for sources associated with the Ophiuchus region are estimated to be between ≈ 0.3 Myr for embedded sources in L1688 region to ≈ 10 Myr for objects in the surface population (Wilking et al. 2008). In Perseus, our survey covered ≈ 1.3 square degrees and included the IC 348 and NGC 1333 clusters, with ages of ~ 2 and ~ 1 Myr, respectively (Young et al. 2015).

4.1. Broad-band J and H Photometry

Broad-band J and H photometry was obtained using UKIRT/WFCAM (Project U/07A/H30), CFHT/WIRCAM (Programs 08AH14 and 07BH20) and Blanco/ISPI (Program 2010A-0326).

The data taken with the UKIRT Wide Field Camera (WFCAM; Casali et al. 2007) use a photometric system described in Hewett et al. (2006), which includes J and H -band filters meeting the Maunakea Observatories (MKO; Simons & Tokunaga 2002; Tokunaga et al. 2002) near-IR filter specifications. The pipeline processing and science archive are described in Irwin et al. (2004) and Hambly et al. (2008), respectively. We used the pipeline-processed photometry tables from stacked images.

For J and H -band data taken with CFHT/WIRCAM, we used pre-processed data from 'Iwi, the CFHT facility pipeline, which includes detrending and sky subtraction. For data taken with Blanco/ISPI, we used custom IDL programs (Allers et al. 2006) to flat field and sky subtract the data. We determined astrometry for our WIRCAM and ISPI fields using astromatic's SCAMP program (Bertin 2006) and then combined data for each pointing using SWARP (Bertin et al. 2002).

We measured photometry using Source Extractor (Bertin, & Arnouts 1996). We determine the photometric calibration for our data using 2MASS (Skrutskie et al. 2006). We first convert the 2MASS photometry for our regions to the MKO system using the conversions of Leggett et al. (2006). In addition, we included J and H band photometry of Ophiuchus from Allers et al. (2006). We then combine all of our broad-band J and H photometry into a master catalog, using a weighted mean to combine photometry for objects detected in more than one field.

4.2. W Photometry

Observations with the W filter were obtained using the ULBCam instrument on the UH 88" Telescope on Maunakea. ULBCam contained a 4096×4096 pixel detector array, configured as a mosaic of four 2048×2048 pixel prototype Hawaii2-RG detectors. The array had a $17' \times 17'$ field of view with a pixel scale of $0''.25$. Four amplifiers were used per detector, with each amplifier controlling 512×2048 pixels.

ULBCam stored every read of the array. We employed a technique whereby we reset the array, took an initial read, read out the array again after 10 s and had a final read of the array 210 s later. We then moved to the next position in our dither sequence, and took another set of three exposures. For a typical field, we used a 13-point dither pattern with offsets of $0'.5$ – $1'.0$ from the initial position. A typical observing sequence resulted in 45 minutes of total integration time. The details of our observations are available in Table 3.

Data reduction for ULBCam data is complicated by many array imperfections. In particular, the array suffered from severe image persistence, an occasionally dead or extremely noisy amplifier, and for our 2008 data, a dead detector. To account for these array imperfections in our data reduction, we construct a master flat field by mean-combining several dome and twilight flats taken during each observing campaign for which the instrument was contiguously installed on the telescope. We also constructed a flat field error frame as the standard deviation of the mean. A bad pixel mask was created by flagging dead pixels and pixels with a flat field uncertainty greater than 10%.

We use custom IDL scripts to create a double-pass sky frame. We first flag saturated pixels in the final read and then subtract the first read from the final read. To determine the uncertainty due to flat field error (σ_{flat}), we multiply each frame by the flat field error frame. We then split each frame (including saturation flag, flat field uncertainty, bad pixel mask and read-subtracted frame) into individual images (of 512×2048 pixels) for each amplifier. We median-zero each image within a set, and create a median-combined initial sky frame which is then subtracted from each image. Using the SExtractor program (Bertin, & Arnouts 1996), we identify stars in each image and save a background rms map (σ_{bkg}). We then create a second-pass sky after masking out the detected stars, and subtract this sky from the images. For each image, we also construct a weight map, where the weight for each pixel is: $w = \frac{\text{badpixelmask}}{\sigma_{\text{bkg}}^2 + \sigma_{\text{flat}}^2}$. Some frames showed significant smearing of point sources, indicative of slight motion of the telescope. These frames were used in the determination of the sky frame but were discarded from the remaining steps in our data reduction process, and are not included in the total integration times listed in Table 3.

To create an astrometric solution for each image, we first re-combine the images from each amplifier to create a multi-extension FITS file where each extension corresponds to an individual amplifier. For each observing semester (2007A, 2008A, and 2008B), we create a global astrometric header and use the SCAMP program (Bertin 2006) to determine the astrometric solution of our images by matching

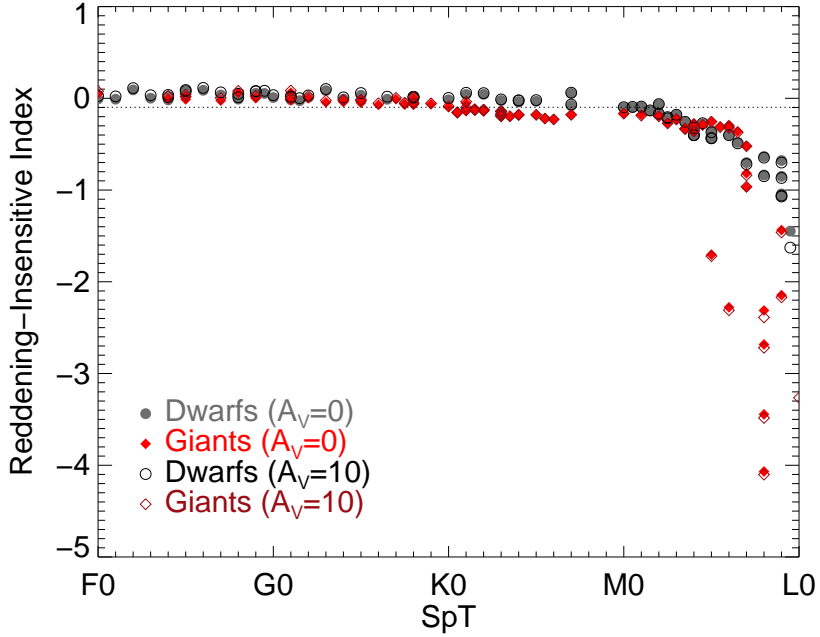


Figure 8. Relation between spectral type and the reddening-insensitive index, Q , calculated from synthesized J , H , and W -band photometry from the SpeX Spectral Library (Cushing et al. 2005; Rayner et al. 2009). The population of background stars is expected to be dominated by late-K and early M dwarfs. The dotted line denotes $Q=-0.098$, which we use to determine the flux zero-point for each of our W -filter images.

to 2MASS H -band detections. The median rms in position for bright detections ($S/N > 100$) relative to positions in the 2MASS catalog was $0''.11$.

The H_2O absorption feature on which we centered our custom filter coincides with a telluric absorption feature. Thus, the throughput of the filter and the photometric zero-point depend on airmass and the atmospheric precipitable water vapor content (see Section 3.3). To determine the W magnitudes of our detected objects, we employ the expected Q values of background stars, which are roughly constant for spectral types earlier than M3 (Figure 8). Galactic population synthesis models (Robin et al. 2003; Girardi et al. 2005) predict that the background population in our images will be dominated by late-K and early-M dwarfs.

So we determine the photometric zero-point for each W image such that the median measured Q agrees with the median predicted Q of the synthesized background (-0.098). Our photometric calibration uncertainties (based on the standard deviation of the mean of measured Q values within an individual frame) range from 0.01 mag for the typical, low extinction regions with many detected stars to 0.05 mag for regions with high extinction and few detected stars.

Because of the array imperfections present in ULBCam data, we did not stack our images, but rather extracted photometry on individual reduced frames using SExtractor. We then combined photometry for individual objects across all of our images using a robust weighted mean. Figure 9 shows the W magnitudes and uncertainties for sources toward IC 348 observed on 2018 November 6.

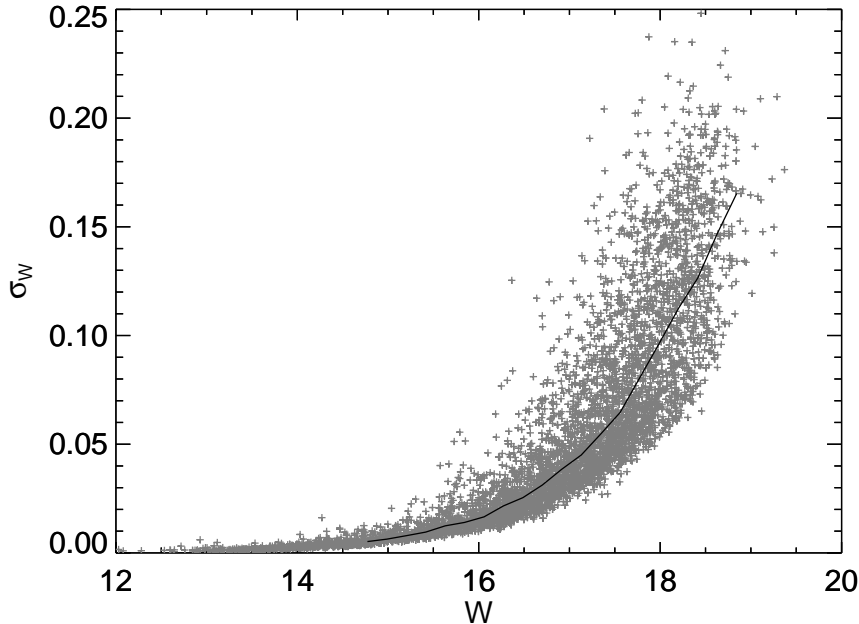


Figure 9. W photometry for IC 348 fields observed on 2018 November 6. The gray points show the final W photometric magnitudes and uncertainties. The solid line shows the median photometric uncertainty as a function of magnitude.

5. SPEX FOLLOWUP OF BROWN DWARF CANDIDATES

We selected our list of candidates *using their Q -values alone*. Although ancillary photometry (optical, Spitzer, and WISE) were available, we chose to rely solely on the combination of J , H , and W photometry to test the efficacy of our custom filter (Table 4). We selected objects having $Q < -0.6$, which should correspond to objects with spectral types later than M6. Figure 10 shows the criteria we used to identify candidates on the $J - W$ versus $W - H$ color plane. Figure 11 compares the broad band colors and magnitudes of our candidates to known members. Overall, our candidates do not have unusual broad band colors compared to previously known members.

We obtained near-IR spectroscopic followup for 60 of our candidate brown dwarfs using the SpeX spectrograph (Rayner et al. 2003) on the NASA Infrared Telescope Facility. The majority of our spectra were obtained using the low-resolution prism mode, which covers the full 0.8–2.5 μm wavelength range at low resolution ($R \sim 75 - 200$). For a few brighter candidates, we used the higher resolution cross-dispersed observing mode ($R \sim 750 - 2000$). Table 5 provides the details of our observations. We observed A0 stars as telluric standards adjacent to our observations of our candidates, and selected the particular standard to provide a good match in sky position (typically within 10°) and airmass (typically within 0.1). For IC 348 and NGC 1333 candidates, we used either HD 22859 or HD 24000 as telluric standards. For Ophiuchus candidates, we used either HD 149827, HD 151787, or HD 153068 as telluric standards. We used SpeXtool version 3.0 (Cushing et al. 2004) to reduce our

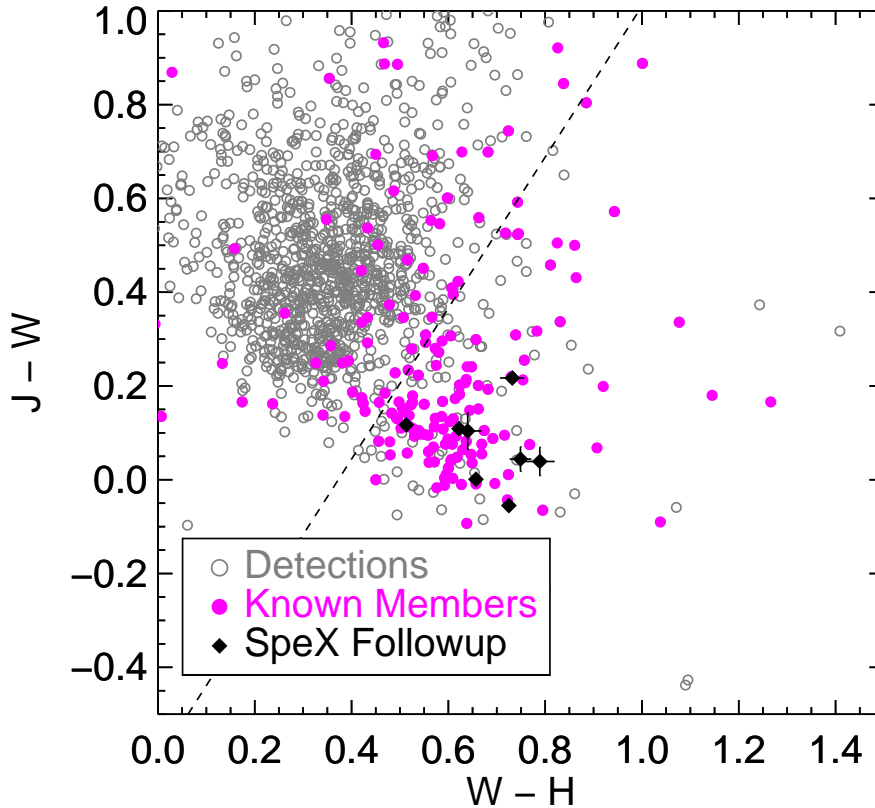


Figure 10. Color-color plot showing our selection criteria for IC 348 fields observed with the W on 2018 November 6. The gray circles show all of the detections in the final photometric catalog. The magenta circles show our photometry for IC 348 members compiled by [Luhman et al. \(2016\)](#). The dashed line indicates a line of constant $Q = -0.6$. We selected candidates for spectroscopic followup that had Q values $> 3\sigma$ below -0.6 , which corresponds to objects which fall $> 3\sigma$ to the right of the dashed line. We obtained spectroscopic followup of 8 of the candidates (black diamonds), all of which were confirmed.

spectra, including correction for telluric absorption following the method described in [Vacca et al. \(2003\)](#).

We classify our spectra using a method similar to that described in [Allers & Liu \(2013\)](#), which includes a gravity-independent determination of near-IR spectral type followed by an index-based gravity classification. Unlike the [Allers & Liu \(2013\)](#) sample, our targets are likely to be attenuated by dust from the star-forming region. Thus, we modified the [Allers & Liu \(2013\)](#) classification method as follows:

- For visual comparison to spectral type standards, we use the VL-G spectral standards presented in [Allers & Liu \(2013\)](#).

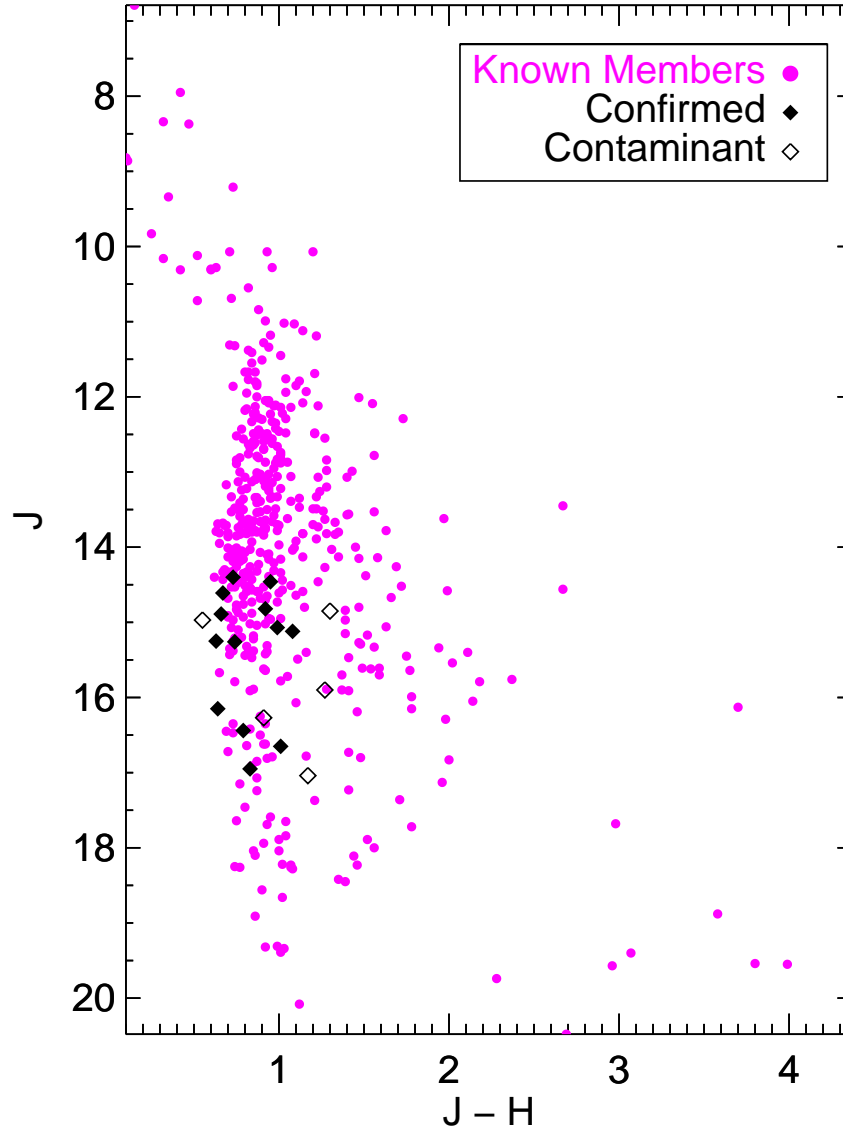


Figure 11. Color-magnitude plot comparing our candidates with spectroscopic followup to known members of IC 348. The magenta circles show photometry for IC 348 members compiled by [Luhman et al. \(2016\)](#). We obtained spectroscopic followup of 18 of the candidates (black diamonds), 13 of which were confirmed as likely IC 138 members (solid diamonds).

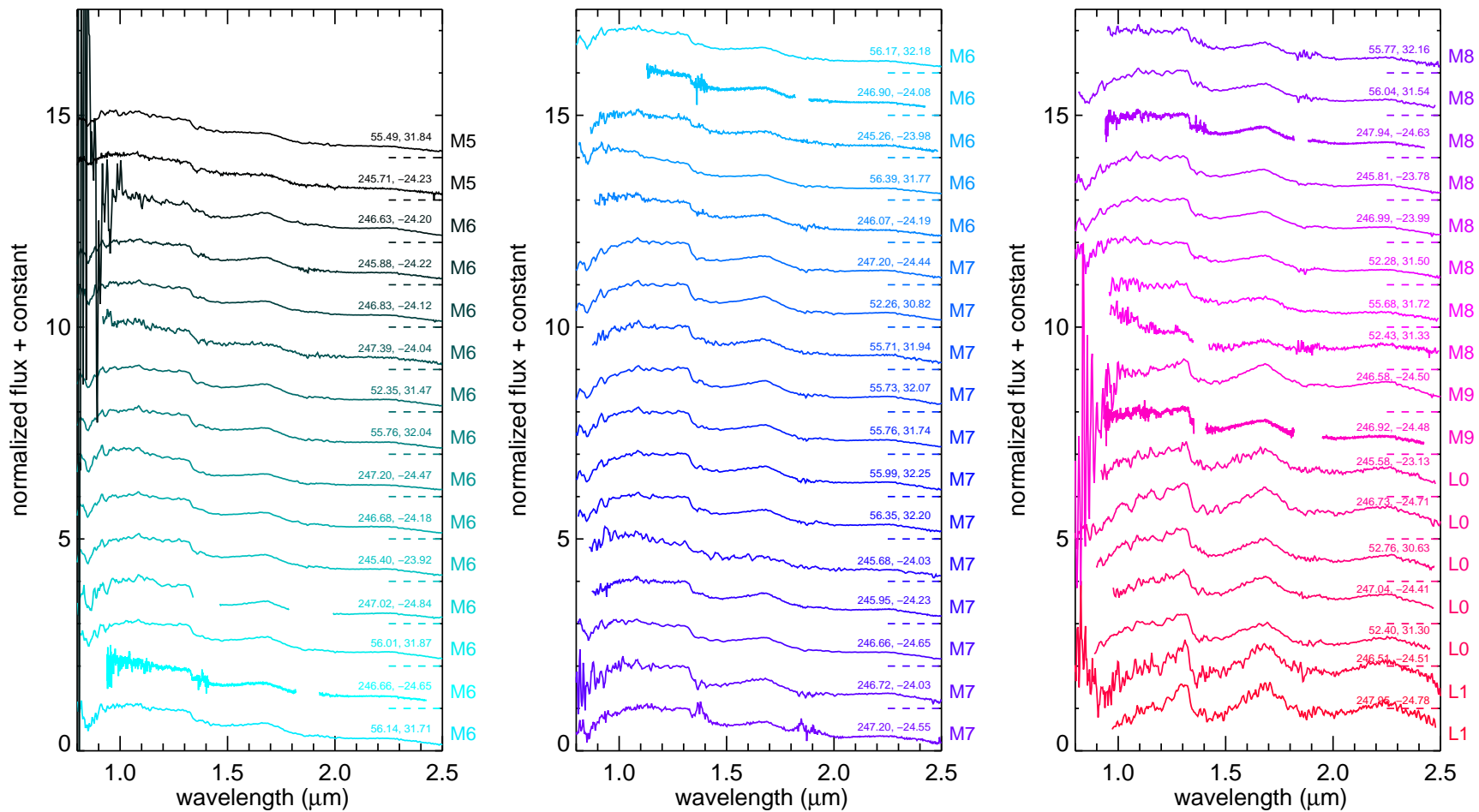


Figure 12. De-reddened spectra of candidate members with spectral types of M5 and later. Spectra have been de-reddened using the reddening law of [Fitzpatrick \(1999\)](#) using the estimated A_V values in Table 6. Spectra are labeled with the decimal coordinates (in degrees) of the candidates.

- While comparing to spectral standards, we first de-redden the spectrum of our candidate so that its synthetic $J - K$ color matches the spectral standard.
- To determine an estimated A_V for our candidates, we use the mean of A_V values needed to match spectral standards that have spectral types within one subtype (the uncertainty of the Allers & Liu (2013) classification) of the best-matching standard.
- We then de-redden the candidate’s spectrum by our A_V estimate, and follow the Allers & Liu (2013) method for determining the overall spectral type and gravity classification (using our earlier determination of visual spectral types).

The spectral types and gravity determinations for our spectra are presented in Table 6, along with the estimated reddening. 21 of our candidates observed with SpeX have spectral classifications available in the literature (see Table 6 for references). The uncertainty of the Allers & Liu (2013) spectral typing method is ± 1 subtype. All but one of our spectral type determinations agree to within 1 subtype of an available literature spectral type, and all agree to within 1.5 subtypes. Our estimate of reddening is likely to be very uncertain, as it depends on the reliability of synthetic photometry for our candidates and standards and assumes that our spectral standards represent intrinsic $J - K$ colors for young objects. As noted in Allers & Liu (2013), however, a modest amount of reddening ($A_V \lesssim 7$ mags) does not affect spectral type or gravity determinations. Figure 12 shows de-reddened spectra of our candidates having spectral types of M5 and later.

6. THE W -BAND FILTER CONFIRMATION RATE

Of the 60 candidates for which we obtained spectra, 48 (80%) are confirmed as having spectral types of M5 or later. The 12 contaminant spectra are relatively featureless at SpeX prism resolution, and do not show spectral shapes that could result in a Q -value below -0.6. Their spectra are consistent with being reddened background stars. Most of our contaminants occur in regions of high extinction, where our W -band photometric calibration technique has high systematic uncertainty due to the relatively few number of background sources.

Since the Q -values of young brown dwarfs and old field objects are similarly dependent on spectral type, the 48 confirmed late-M and L type objects are not necessarily members of the coincident star-forming regions. Using the method of Allers & Liu (2013), we also calculated gravity scores from our spectra. Young objects in star-forming regions are expected to have gravity scores of VL-G. Of the 48 confirmed late-type objects, 40 are classified as VL-G, 5 as INT-G, and 1 as FLD-G. Two objects, with spectral types of M5, are unable to have their gravities classified using their low-resolution spectra and the method of Allers & Liu (2013).

We also list the GAIA DR2 parallaxes and proper motions for candidate members in table 6. Of the 22 VL-G-classified spectra having GAIA parallaxes, 21 have parallaxes consistent (to within 2σ) with known members of their respective star-forming regions. Of the three INT-G-classified spectra having GAIA parallaxes, 2 have parallaxes consistent with their respective star-forming regions. In total, we have 43 objects having spectral types of M5 and later with gravity classifications of VL-G or parallaxes consistent with membership, and 4 objects having late-type spectra but uncertain membership. Overall, the confirmation rate from our SpeX survey is 80% if we consider late-type objects, and 72% if we consider only objects with gravity classifications or parallax consistent with membership in their natal star-forming regions.

The regions we surveyed with the W filter have long been known to contain brown dwarfs (see references in Table 6 for examples). When we created our target list for SpeX spectroscopic followup, we omitted 47 known brown dwarfs that met our W -band selection criteria. Thus, if we had done a blind spectroscopic survey, we would have potentially confirmed those 47 known brown dwarfs (in addition to the 43 confirmed in our spectroscopic sample), which would imply an overall confirmation rate of 89% (for objects later than M5) and 84% for objects with gravity classifications or parallax consistent with membership. Our confirmation rate is comparable to the best performance ($\approx 80\%$) achieved from high-quality surveys that use many more photometric bands (e.g., Peña Ramírez et al. 2012; Zapatero Osorio et al. 2017) and include proper-motion selection (e.g., Lodieu et al. 2018). For a survey with selection criteria determined by only 3 photometric bands, our confirmation rate is outstanding.

7. CONCLUSIONS

To search for brown dwarfs in star-forming regions, we have designed the W -band filter, a medium-bandpass filter centered at $1.45 \mu\text{m}$. Our W -band filter can be combined with broad-band J and H photometry to create a reddening-insensitive index, Q . Since the W -band filter is centered on a deep atmospheric water absorption feature seen in the spectra of objects with spectral types of M5 and later, it is able to break the degeneracy in broad-band colors of young brown dwarfs and reddened background stars. The combination of J , H , and W photometry can determine the spectral types of brown dwarfs to within 1.4 subtypes, independent of reddening.

We tested the efficacy of our filter by selecting candidate young brown dwarfs based only on their Q values. Using SpeX, we spectroscopically confirm 48/60 objects as having spectral types of M5 and later. If we include objects that met our selection criteria but were already spectroscopically confirmed prior to our SpeX observations, our confirmation rate is 95/107. The high confirmation rate of our survey demonstrates the ability of custom near-IR filters to identify young brown dwarfs. Our spectroscopic confirmation includes seven objects with spectral types of L0 or later (3 of which are new discoveries), making them among the lowest mass confirmed members of star-forming regions.

Based on the success of our pilot survey with the W filter, we subsequently collaborated on the installation of a similar filter on the Canada France Hawai'i Telescope's Wide-Field IR camera. The first discoveries from this CFHT survey of Serpens have been recently reported (Jose et al. 2020), providing further confirmation of the effectiveness of the W -filter selection, even for star-forming regions near the Galactic Plane.

ACKNOWLEDGMENTS

This publication makes use of data products from the Two Micron All Sky Survey, which is a joint project of the University of Massachusetts and the Infrared Processing and Analysis Center/California Institute of Technology, funded by the National Aeronautics and Space Administration and the National Science Foundation. This research has benefited from the SpeX Prism Spectral Libraries, maintained by Adam Burgasser at <http://pono.ucsd.edu/~adam/browndwarfs/spexprism>. We thank John Rayner and Shane Jacobson for assisting with design and installation of the *W*-band filter. We are grateful to Geoff Mathews and Mark Pitts for conducting some of the SpeX observations. Zhoujian Zhang and Michael Gully-Santiago provided useful conversations which improved this manuscript. We are grateful to members of the *W* filter collaboration for sharing ideas on data reduction, analysis, and scientific results. KNA thanks Greg Herczeg and the Kavli Institute for Astronomy and Astrophysics at Peking University for supporting a collaborative visit. This work benefited from the 2019 Exoplanet Summer Program in the Other Worlds Laboratory (OWL) at the University of California, Santa Cruz, a program funded by the Heising-Simons Foundation. This work was supported by NSF grant AST-0407441. Support for program numbers 15238 and 15628 was provided through a grant from the STScI under NASA contract NAS5-26555.

REFERENCES

- Allers, K. N., Kessler-Silacci, J. E., Cieza, L. A., et al. 2006, *ApJ*, 644, 364
- Allers, K. N., & Liu, M. C. 2013, *ApJ*, 772, 79
- Allers, K. N., Liu, M. C., Shkolnik, E., et al. 2009, *ApJ*, 697, 824
- Alves de Oliveira, C., Moraux, E., Bouvier, J., et al. 2010, *A&A*, 515, A75
- Alves de Oliveira, C., Moraux, E., Bouvier, J., & Bouy, H. 2012, *A&A*, 539, A151
- Alves de Oliveira, C., Moraux, E., Bouvier, J., et al. 2013, *A&A*, 549, A123
- Barsony, M., Haisch, K. E., Marsh, K. A., & McCarthy, C. 2012, *ApJ*, 751, 22
- Basri, G., Marcy, G. W., & Graham, J. R. 1996, *ApJ*, 458, 600
- Bertin, E., & Arnouts, S. 1996, *A&AS*, 117, 393
- Bertin, E., Mellier, Y., Radovich, M., et al. 2002, *adass*, 281, 228
- Bertin, E. 2006, *adass XV*, 351, 112
- Bessell, M. S. 2005, *ARA&A*, 43, 293
- Bohlin, R. C. 2007, *ASPC* 364, *The Future of Photometric, Spectrophotometric and Polarimetric Standardization*, ed. C. Sterken (San Francisco, CA: ASP), 315
- Briceño, C., Luhman, K. L., Hartmann, L., Stauffer, J. R., & Kirkpatrick, J. D. 2002, *ApJ*, 580, 317
- Burgasser, A. J. 2014 arXiv:1406.4887
- Cánovas, H., Cantero, C., Cieza, L., et al. 2019, *A&A*, 626, A80
- Casali, M., Adamson, A., Alves de Oliveira, C., et al. 2007, *A&A*, 467, 777
- Cushing, M. C., Rayner, J. T., & Vacca, W. D. 2005, *ApJ*, 623, 1115
- Cushing, M. C., Vacca, W. D., & Rayner, J. T. 2004, *PASP*, 116, 362
- Faherty, J. K., Riedel, A. R., Cruz, K. L., et al. 2016, *ApJS*, 225, 10
- Fiorucci, M., & Munari, U. 2003, *A&A*, 401, 781
- Fitzpatrick, E. L. 1999, *PASP*, 111, 63
- Geers, V., Scholz, A., Jayawardhana, R., et al. 2011, *ApJ*, 726, 23
- Girardi, L., Groenewegen, M. A. T., Hatziminaoglou, E., et al. 2005, *A&A*, 436, 895
- Hambly, N. C., Collins, R. S., Cross, N. J. G., et al. 2008, *MNRAS*, 384, 637
- Herczeg, G. J., & Hillenbrand, L. A. 2014, *ApJ*, 786, 97
- Hewett, P. C., Warren, S. J., Leggett, S. K., et al. 2006, *MNRAS*, 367, 454
- Irwin, M. J., Lewis, J., Hodgkin, S., et al. 2004, *Proc. SPIE*, 5493, 411
- Johnson, H. L., & Morgan, W. W. 1953, *ApJ*, 117, 313

- Jose, J., Biller, B. A., Albert, L., et al. 2020, *ApJ*, 892, 122
- Kirkpatrick, J. D., Looper, D. L., Burgasser, A. J., et al. 2010, *ApJS*, 190, 100
- Leggett, S. K., Currie, M. J., Varricatt, W. P., et al. 2006, *MNRAS*, 373, 781
- Liu, M. C., Dupuy, T. J., & Allers, K. N. 2013, *AN*, 334, 85
- Liu, M. C., Dupuy, T. J., & Allers, K. N. 2016, *ApJ*, 833, 96
- Liu, M. C., Najita, J., & Tokunaga, A. T. 2003, *ApJ*, 585, 372
- Lodieu, N., Dobbie, P. D., Cross, N. J. G., Hambly, N. C., Read, M. A. 2013, *MNRAS*, 435, 2474
- Lodieu, N., Zapatero Osorio, M. R., Béjar, V. J. S., et al. 2018, *MNRAS*, 473, 2020
- Lord, S.D. 1992, NASA Technical Memor. 103957
- Luhman, K. L., Esplin, T. L., & Loutrel, N. P. 2016, *ApJ*, 827, 52
- Luhman, K. L., & Mamajek, E. E. 2012, *ApJ*, 758, 31
- Luhman, K. L., Rieke, G. H., Lada, C. J., et al. 1998, *ApJ*, 508, 347
- Mainzer, A. K., & McLean, I. S. 2003, *ApJ*, 597, 555
- Martín, E. L., Rebolo, R. & Zapatero-Osorio, M. 1996, *ApJ*, 469, 706
- Martín, E. L., Basri, G., Gallegos, J. E., et al. 1998, *ApJL*, 499, L61
- Megessier, C. 1995, *A&A*, 296, 771
- Muench, A. A., Lada, C. J., Luhman, K. L., Muzerolle, J., & Young, E. 2007, *AJ*, 134, 411
- Mužić, K., Scholz, A., Geers, V., Jayawardhana, R., & Tamura, M. 2012, *ApJ*, 744, 134
- Najita, J. R., Tiede, G. P., & Carr, J. S. 2000, *ApJ*, 541, 977
- Ortiz-León, G. N., Loinard, L., Dzib, S. A., et al. 2018, *ApJ*, 865, 73
- Peña Ramírez, K., Béjar, V. J. S., Zapatero Osorio, M. R., et al. 2012, *ApJ*, 754, 30
- Rayner, J. T., Cushing, M. C., & Vacca, W. D. 2009, *ApJS*, 185, 289
- Rayner, J. T., Toomey, D. W., Onaka, P. M., et al. 2003, *PASP*, 115, 362
- Rebolo, R., Zapatero Osorio, M. R., Madrugá, S., et al. 1998, *Sci*, 282, 1309
- Robin, A. C., Reylé, C., Derrière, S., & Picaud, S. 2003, *A&A*, 409, 523
- Rosenthal, E. D., Gurwell, M. A., & Ho, P. T. P. 1996, *Nature*, 384, 243
- Scholz, A., Geers, V., Jayawardhana, R., et al. 2009, *ApJ*, 702, 805
- Scholz, A., Jayawardhana, R., Muzic, K., et al. 2012, *ApJ*, 756, 24
- Simons, D. A., & Tokunaga, A. 2002, *PASP*, 114, 169
- Skrutskie, M. F., Cutri, R. M., Stiening, R., et al. 2006, *AJ*, 131, 1163
- Slesnick, C. L., Carpenter, J. M., & Hillenbrand, L. A. 2006, *AJ*, 131, 3016
- Slesnick, C. L., Hillenbrand, L. A., & Carpenter, J. M. 2008, *ApJ*, 688, 377
- Strömgren, B. 1966, *ARA&A*, 4, 433
- Testi, L. 2009, *A&A*, 503, 639
- Tinney, C. G., Burgasser, A. J., Kirkpatrick, J. D., & McElwain, M. W. 2005, *AJ*, 130, 2326
- Tokunaga, A. T., Simons, D. A., & Vacca, W. D. 2002, *PASP*, 114, 180
- Tokunaga, A. T., & Vacca, W. D. 2005, *PASP*, 117, 421
- Vacca, W. D., Cushing, M. C., & Rayner, J. T. 2003, *PASP*, 115, 389
- Wilking, B. A., Gagné, M., & Allen, L. E. 2008, in *Handbook of Star Forming Regions, Volume II: The Southern Sky*, ed. B. Reipurth (San Francisco, CA: ASP), 351
- Wilking, B. A., Meyer, M. R., Greene, T. P., et al. 2004, *AJ*, 127, 1131
- Wilking, B. A., Meyer, M. R., Robinson, J. G., & Greene, T. P. 2005, *AJ*, 130, 1733
- Young, K. E., Young, C. H., Lai, S.-P., et al. 2015, *AJ*, 150, 40
- Zapatero Osorio, M. R., Béjar, V. J. S., & Peña Ramírez, K. 2017, *ApJ*, 842, 65

Table 3. Observing Log: *W* Band Imaging

Position	Date	sec <i>z</i>	T_{int}	Seeing
	(UT)		(minutes)	(arcsec)
16 27 46.6 -24 25 38	2007 May 22	1.47	45.5	0.9
16 27 46.6 -24 07 24	2007 May 22	1.39	45.5	1.2
16 26 28.8 -24 25 24	2007 May 22	1.48	45.5	0.8
16 26 28.8 -24 08 38	2007 May 22	1.67	45.5	1.2
16 26 28.8 -24 43 34	2007 May 24	1.46	73.5	1.0
16 27 46.6 -24 42 30	2007 May 24	1.53	91.0	0.9
16 23 03.0 -23 37 56	2007 May 24	2.00	31.5	1.2
16 23 03.0 -23 39 14	2007 May 26	1.50	42.0	1.3
16 23 03.3 -24 12 20	2007 May 26	1.53	56.0	1.5
16 23 03.2 -23 55 10	2007 May 26	1.55	80.5	1.5
16 21 46.0 -23 56 56	2007 May 27	1.59	45.5	1.2
16 22 07.0 -23 31 44	2007 May 27	1.40	45.5	1.4
16 22 07.0 -23 14 41	2007 May 27	1.46	84.0	1.1
16 29 04.3 -24 42 34	2007 May 27	1.89	45.5	1.2
16 29 04.3 -24 26 34	2007 May 29	1.75	45.5	1.2
16 31 54.0 -24 47 39	2007 May 29	1.50	45.5	1.2
16 33 12.0 -24 48 20	2007 May 29	1.41	45.5	1.3
16 31 54.0 -24 29 57	2007 May 29	1.45	45.5	1.2
16 33 12.0 -24 28 41	2007 May 29	1.73	63.0	1.1
16 33 12.2 -24 12 39	2007 Jun 3	1.70	42.0	1.2
16 31 54.0 -24 11 57	2007 Jun 3	1.48	45.5	1.1
16 34 30.0 -24 48 09	2007 Jun 3	1.41	45.5	1.3
16 34 30.8 -24 29 03	2007 Jun 3	1.44	28.0	1.1
16 34 30.0 -24 11 11	2007 Jun 3	1.64	45.5	1.1
16 21 46.0 -24 14 16	2007 Jun 23	1.47	45.5	1.2
16 20 51.6 -23 15 00	2007 Jun 23	1.37	42.0	1.2
16 20 52.0 -23 32 09	2007 Jun 23	1.46	45.5	1.2
16 21 46.0 -23 39 02	2007 Jun 23	1.74	45.5	1.3
16 26 28.8 -24 47 07	2008 Jun 13	1.48	63.0	1.5
16 29 04.3 -24 11 25	2008 Jun 13	1.41	59.5	1.7
16 25 19.0 -24 48 23	2008 Jun 13	1.65	45.5	1.7
16 25 19.0 -24 39 15	2008 Jun 14	1.62	42.0	1.2
16 25 19.0 -24 30 18	2008 Jun 14	1.44	45.5	1.3
16 25 19.0 -24 21 25	2008 Jun 14	1.40	45.5	1.2
16 25 19.0 -24 12 39	2008 Jun 14	1.51	45.5	1.2
16 25 19.0 -24 04 16	2008 Jun 14	1.82	45.5	1.8
16 24 06.0 -24 48 16	2008 Jun 18	1.66	35.0	1.2
16 24 06.0 -24 30 52	2008 Jun 18	1.46	45.5	1.4
16 24 06.0 -24 12 52	2008 Jun 18	1.40	45.5	1.1
16 24 06.0 -23 55 09	2008 Jun 18	1.49	45.5	1.0
16 24 06.0 -24 04 15	2008 Jun 18	1.67	17.5	1.3
16 24 06.0 -24 39 28	2008 Jun 19	1.65	38.5	1.2
16 24 06.0 -24 21 56	2008 Jun 19	1.45	45.5	1.2

Table 3 continued on next page

Table 3 (*continued*)

Position	Date	sec z	T_{int}	Seeing
	(UT)		(minutes)	(arcsec)
03 41 55.0 +31 33 34	2008 Aug 15	1.20	45.5	1.3
03 43 10.0 +31 33 37	2008 Aug 15	1.09	45.5	1.0
03 44 25.0 +31 33 02	2008 Aug 17	1.44	45.5	1.1
03 45 40.0 +31 33 34	2008 Aug 17	1.19	45.5	1.1
03 41 55.0 +31 49 32	2008 Aug 17	1.07	45.5	1.0
03 28 50.0 +31 07 54	2008 Oct 19	1.66	45.5	0.9
03 30 00.0 +31 07 46	2008 Oct 19	1.34	45.5	1.1
03 28 50.0 +31 17 29	2008 Oct 19	1.15	45.5	0.9
03 30 00.0 +31 17 43	2008 Oct 19	1.06	45.5	1.1
03 31 10.0 +31 08 05	2008 Oct 19	1.02	45.5	1.1
03 31 10.0 +31 17 39	2008 Oct 19	1.04	45.5	1.0
03 28 50.0 +30 58 42	2008 Oct 19	1.12	45.5	1.0
03 30 00.0 +30 58 44	2008 Oct 19	1.27	45.5	1.0
03 31 10.2 +30 58 46	2008 Oct 19	1.51	42.0	1.1
03 43 09.0 +31 55 34	2008 Nov 6	1.51	45.5	0.7
03 44 26.0 +31 55 59	2008 Nov 6	1.25	45.5	0.7
03 45 44.0 +31 55 47	2008 Nov 6	1.10	45.5	0.7
03 43 09.0 +32 06 00	2008 Nov 6	1.74	56.0	0.7
03 44 26.0 +32 04 54	2008 Nov 6	1.40	45.5	0.7
03 45 44.0 +32 04 55	2008 Nov 6	1.18	45.5	0.7
03 43 09.0 +32 14 14	2008 Nov 6	1.06	45.5	0.8
03 44 26.0 +32 14 27	2008 Nov 6	1.03	45.5	0.8
03 45 44.0 +32 14 40	2008 Nov 6	1.04	45.5	0.8
03 43 09.0 +31 44 10	2008 Nov 15	1.50	45.5	0.7
03 44 26.0 +31 45 29	2008 Nov 15	1.21	45.5	0.7
03 45 43.6 +31 45 50	2008 Nov 15	1.09	42.0	0.7
03 43 27.0 +32 24 20	2008 Nov 15	1.03	45.5	0.8
03 44 37.0 +32 23 59	2008 Nov 15	1.03	45.5	0.8
03 45 47.0 +32 24 09	2008 Nov 15	1.08	45.5	0.9
03 28 50.0 +30 52 04	2008 Nov 15	1.25	45.5	0.7
03 30 00.0 +30 51 56	2008 Nov 15	1.49	45.5	0.7
03 31 10.0 +30 48 40	2008 Nov 16	1.56	45.5	1.1
03 28 50.0 +30 39 39	2008 Nov 16	1.24	45.5	1.1
03 30 00.0 +30 39 40	2008 Nov 16	1.10	45.5	1.1
03 31 10.0 +30 39 33	2008 Nov 16	1.03	45.5	1.2
03 28 50.0 +30 30 24	2008 Nov 16	1.02	45.5	1.1
03 30 00.0 +30 30 32	2008 Nov 16	1.07	45.5	1.2
03 31 10.0 +30 30 27	2008 Nov 16	1.17	45.5	1.1

Table 4. Photometry of Observed Brown Dwarf Candidates

Object	W	J_{MKO}	H_{MKO}	$J_{2\text{MASS}}$	$H_{2\text{MASS}}$	Q_{MKO}	$Q_{2\text{MASS}}$
	(mag)	(mag)	(mag)	(mag)			
NGC 1333							
UHW J052.25592+30.82075	13.51±0.02	13.49±0.01	12.99±0.01	13.53±0.03	12.89±0.03	-0.86±0.05	-0.92±0.07
UHW J052.26618+30.94156	15.82±0.04	15.94±0.01	15.15±0.01	15.64±0.06	14.64±0.07	-0.96±0.10	-1.98±0.16
UHW J052.27886+31.49911	16.28±0.05	16.33±0.01	15.53±0.01	16.68±0.05	15.52±0.05	-1.16±0.13	-0.76±0.15
UHW J052.30643+31.39637	17.09±0.05	17.04±0.02	16.18±0.01	...	16.10±0.07	-1.51±0.14	...
UHW J052.35191+31.47077	13.84±0.04	13.88±0.01	13.18±0.01	14.06±0.02	13.19±0.02	-1.03±0.11	-0.78±0.11
UHW J052.40147+31.29717	17.92±0.05	17.77±0.01	17.15±0.01	17.92±0.15	17.12±0.22	-1.39±0.12	-1.22±0.39
UHW J052.43392+31.32982	17.40±0.03	17.58±0.01	16.52±0.01	17.45±0.09	...	-1.24±0.08	...
UHW J052.75599+30.63090	16.43±0.03	16.30±0.01	15.60±0.01	16.57±0.16	15.85±0.18	-1.47±0.08	-0.76±0.34
IC 348							
UHW J055.48646+31.83838	15.08±0.02	14.97±0.01	14.42±0.01	15.06±0.04	14.36±0.05	-1.16±0.05	-1.10±0.10
UHW J055.54657+31.94999	15.66±0.04	15.90±0.01	14.63±0.01	16.10±0.09	14.65±0.06	-1.42±0.10	-1.10±0.16
UHW J055.55875+31.95973	14.53±0.02	14.85±0.01	13.55±0.01	14.97±0.04	13.57±0.04	-1.24±0.06	-1.01±0.09
UHW J055.67611+31.72142	16.37±0.03	16.65±0.03	15.64±0.01	16.77±0.13	15.49±0.10	-0.90±0.08	-0.94±0.21
UHW J055.71237+31.94127	16.37±0.04	16.44±0.01	15.65±0.01	16.59±0.11	15.54±0.12	-1.09±0.11	-1.03±0.25
UHW J055.73277+32.07455	14.73±0.03	14.61±0.01	13.94±0.01	14.76±0.02	13.99±0.02	-1.38±0.07	-1.08±0.08
UHW J055.75603+32.03731	14.34±0.02	14.40±0.01	13.67±0.01	14.49±0.02	13.68±0.02	-1.02±0.06	-0.86±0.07
UHW J055.75810+31.74320	14.77±0.03	14.82±0.01	13.90±0.01	14.91±0.04	13.93±0.04	-1.34±0.08	-1.13±0.11
UHW J055.76964+32.16007	16.90±0.03	16.95±0.01	16.12±0.01	17.06±0.06	16.03±0.07	-1.20±0.08	-1.15±0.15
UHW J055.98976+32.24691	14.83±0.02	14.89±0.01	14.23±0.01	14.96±0.02	14.23±0.03	-0.91±0.05	-0.79±0.06
UHW J056.01221+31.87436	14.23±0.02	14.46±0.01	13.51±0.03	14.71±0.03	13.57±0.03	-0.94±0.05	-0.53±0.06
UHW J056.04265+31.54385	16.15±0.03	16.15±0.01	15.51±0.01	16.29±0.11	15.33±0.09	-1.03±0.07	-1.11±0.19
UHW J056.07487+31.58792	16.83±0.03	17.04±0.01	15.87±0.01	16.69±0.15	15.91±0.16	-1.33±0.07	-1.53±0.30
UHW J056.14403+31.71225	14.83±0.02	15.07±0.03	14.08±0.03	15.23±0.05	14.08±0.03	-0.96±0.08	-0.74±0.09
UHW J056.17321+32.17758	15.17±0.03	15.25±0.01	14.62±0.01	15.39±0.03	14.68±0.03	-0.81±0.07	-0.52±0.09
UHW J056.34957+32.19849	15.09±0.02	15.26±0.04	14.52±0.03	15.33±0.02	14.48±0.03	-0.74±0.06	-0.68±0.05
UHW J056.37556+31.62740	16.25±0.02	16.27±0.01	15.36±0.01	16.43±0.13	15.26±0.08	-1.41±0.05	-1.33±0.18
UHW J056.38941+31.76537	14.96±0.03	15.12±0.01	14.04±0.01	15.26±0.05	14.00±0.04	-1.32±0.07	-1.17±0.10
Ophiuchus							
UHW J245.25929-23.97766	14.40±0.02	14.63±0.01	13.80±0.01	14.75±0.04	13.79±0.03	-0.76±0.05	-0.59±0.05
UHW J245.32623-23.90277	17.22±0.02	17.60±0.04	16.42±0.02	-0.92±0.08	...
UHW J245.39963-23.91766	13.82±0.02	13.79±0.01	13.16±0.01	13.95±0.03	13.19±0.02	-1.09±0.05	-0.82±0.05
UHW J245.48320-23.35050	11.48±0.02	11.50±0.03	10.50±0.02	...	-1.47±0.05
UHW J245.58499-23.13122	16.59±0.02	16.95±0.18	15.42±0.12	...	-1.42±0.27
UHW J245.66849-23.56412	12.32±0.02	12.72±0.02	11.48±0.02	...	-0.88±0.05
UHW J245.68198-24.03424	17.04±0.03	17.32±0.01	16.30±0.01	-0.90±0.07	...
UHW J245.71139-24.22963	15.39±0.02	15.47±0.01	14.92±0.01	15.46±0.05	14.83±0.07	-0.67±0.05	-0.78±0.12
UHW J245.81343-23.78480	14.98±0.02	15.10±0.01	14.21±0.01	15.19±0.04	14.20±0.05	-1.13±0.06	-0.97±0.11
UHW J245.87762-24.22221	11.76±0.02	11.93±0.02	11.01±0.02	...	-0.97±0.05
UHW J245.95168-24.22649	13.04±0.02	13.53±0.03	12.17±0.03	...	-0.84±0.05
UHW J246.06631-24.18753	13.48±0.05	13.83±0.01	12.76±0.01	13.97±0.03	12.79±0.02	-0.81±0.13	-0.57±0.13

Table 4 continued on next page

Table 4 (continued)

Object	W	J_{MKO}	H_{MKO}	$J_{2\text{MASS}}$	$H_{2\text{MASS}}$	Q_{MKO}	$Q_{2\text{MASS}}$
	(mag)	(mag)	(mag)	(mag)			
UHW J246.51367–24.50719	17.50±0.06	17.85±0.02	16.56±0.02	17.68±0.17	16.18±0.10	-1.16±0.16	-1.83±0.28
UHW J246.57742–24.49763	16.41±0.03	17.23±0.02	15.11±0.02	17.36±0.13	15.01±0.04	-1.26±0.08	-1.18±0.16
UHW J246.62661–24.20326	15.05±0.02	16.18±0.02	13.83±0.02	16.32±0.05	13.80±0.02	-0.85±0.05	-0.65±0.06
UHW J246.65753–24.65089	14.41±0.02	14.85±0.02	13.68±0.01	14.93±0.03	13.59±0.02	-0.75±0.05	-0.73±0.05
UHW J246.68094–24.17893	13.31±0.02	13.60±0.02	12.68±0.02	...	-0.66±0.05
UHW J246.71774–24.02967	15.72±0.02	16.08±0.01	14.90±0.01	16.08±0.04	14.83±0.04	-0.97±0.05	-1.00±0.09
UHW J246.73470–24.71048	17.45±0.06	17.56±0.02	16.62±0.02	17.77±0.19	16.59±0.14	-1.24±0.15	-0.99±0.33
UHW J246.82722–24.12273	14.30±0.02	14.73±0.01	13.58±0.01	14.83±0.02	13.55±0.02	-0.72±0.05	-0.60±0.05
UHW J246.90062–24.08269	13.74±0.02	14.11±0.02	12.91±0.03	14.29±0.02	12.95±0.02	-0.97±0.06	-0.65±0.05
UHW J246.92017–24.48353	14.53±0.02	14.64±0.02	13.86±0.02	14.71±0.02	13.78±0.02	-0.98±0.05	-0.96±0.05
UHW J246.94784–24.82865	16.38±0.04	16.56±0.05	15.51±0.05	...	-1.16±0.15
UHW J246.99312–23.98747	13.95±0.02	14.11±0.02	13.28±0.02	14.22±0.02	13.20±0.02	-0.92±0.05	-0.87±0.05
UHW J247.01994–24.84319	13.86±0.02	13.91±0.02	13.09±0.01	13.94±0.02	12.98±0.02	-1.18±0.05	-1.24±0.05
UHW J247.04356–24.40568	17.32±0.04	17.78±0.02	16.28±0.01	...	16.19±0.09	-1.22±0.11	...
UHW J247.19598–24.47051	13.35±0.02	13.24±0.03	12.53±0.02	...	-1.35±0.05
UHW J247.20293–24.44216	14.35±0.02	14.45±0.03	13.67±0.03	...	-0.95±0.07
UHW J247.20293–24.55216	16.56±0.02	17.19±0.01	16.08±0.01	-0.13±0.06	...
UHW J247.38539–24.04299	16.50±0.03	16.82±0.15	15.59±0.10	...	-1.07±0.24
UHW J247.94088–24.62855	12.73±0.07	13.09±0.02	11.85±0.02	...	-0.98±0.17
UHW J247.95427–24.78060	17.55±0.08	17.65±0.01	16.61±0.03	-1.42±0.21	...
UHW J248.69073–24.82275	16.05±0.02	16.25±0.01	15.50±0.02	16.09±0.09	15.27±0.09	-0.70±0.05	-1.15±0.18

Table 5. IRTF/SpeX Observing Log

Object	UT Date	Grat	Slit (")	R	sec z	$N_{\text{exp}} \times t$ (s)	T_{int} (s)	$\langle S/N \rangle$ (Y, J, H, K)
UHW J052.26618+30.94156	2009 Sep 30	LowRes15	0.5×15	120	1.25	10×120.0	1200.0	30, 45, 45, 40
UHW J052.27886+31.49911	2009 Sep 29	LowRes15	0.5×15	120	1.29	10×180.0	1800.0	47, 102, 95, 85
UHW J052.30643+31.39637	2009 Sep 30	LowRes15	0.5×15	120	1.10	12×180.0	2160.0	2, 7, 19, 30
UHW J052.35191+31.47077	2009 Oct 1	LowRes15	0.5×15	120	1.38	10×60.0	600.0	135, 255, 244, 181
UHW J052.40147+31.29717	2009 Sep 28	LowRes15	0.8×15	75	1.09	26×180.0	4680.0	30, 62, 46, 43
UHW J052.43392+31.32982	2009 Sep 29	LowRes15	0.5×15	120	1.11	12×180.0	2160.0	21, 37, 42, 63
UHW J052.75599+30.63090	2009 Sep 28	LowRes15	0.5×15	120	1.02	18×120.0	2160.0	37, 76, 60, 48
UHW J055.48646+31.83838	2009 Oct 1	LowRes15	0.5×15	120	1.27	10×120.0	1200.0	117, 168, 124, 79
UHW J055.54657+31.94999	2009 Sep 28	LowRes15	0.5×15	120	1.10	11×60.0	660.0	17, 45, 59, 44
UHW J055.55875+31.95973	2009 Sep 27	LowRes15	0.5×15	120	1.13	10×60.0	600.0	35, 108, 168, 118
UHW J055.67611+31.72142	2009 Oct 2	LowRes15	0.5×15	120	1.15	16×180.0	2880.0	14, 37, 36, 37
UHW J055.71237+31.94127	2009 Oct 2	LowRes15	0.5×15	120	1.03	16×180.0	2880.0	31, 62, 47, 41
UHW J055.73277+32.07455	2009 Sep 27	LowRes15	0.5×15	120	1.04	10×60.0	600.0	126, 234, 215, 148
UHW J055.75603+32.03731	2009 Oct 2	LowRes15	0.5×15	120	1.16	11×60.0	660.0	98, 193, 165, 134
UHW J055.75810+31.74320	2009 Sep 27	LowRes15	0.5×15	120	1.39	10×120.0	1200.0	103, 228, 210, 194
UHW J055.76964+32.16007	2009 Sep 27	LowRes15	0.5×15	120	1.06	13×180.0	2340.0	28, 66, 66, 47
UHW J055.98976+32.24691	2009 Sep 28	LowRes15	0.5×15	120	1.40	10×60.0	600.0	85, 154, 123, 90
UHW J056.01221+31.87436	2009 Oct 2	LowRes15	0.5×15	120	1.32	10×90.0	900.0	63, 144, 148, 137
UHW J056.04265+31.54385	2009 Sep 27	LowRes15	0.5×15	120	1.02	10×180.0	1800.0	63, 118, 95, 59
UHW J056.07487+31.58792	2009 Sep 28	LowRes15	0.5×15	120	1.20	12×180.0	2160.0	16, 35, 43, 33
UHW J056.14403+31.71225	2009 Oct 1	LowRes15	0.5×15	120	1.15	16×120.0	1920.0	43, 114, 118, 115
UHW J056.17321+32.17758	2009 Oct 2	LowRes15	0.5×15	120	1.08	12×120.0	1440.0	96, 162, 122, 97
UHW J056.34957+32.19849	2009 Sep 28	LowRes15	0.5×15	120	1.08	10×60.0	600.0	60, 120, 103, 79
UHW J056.37556+31.62740	2009 Sep 27	LowRes15	0.5×15	120	1.08	9×180.0	1620.0	41, 76, 75, 50
UHW J056.38941+31.76537	2009 Sep 27	LowRes15	0.5×15	120	1.19	10×120.0	1200.0	67, 167, 195, 178
UHW J245.25929−23.97766	2012 Jul 5	LowRes15	0.5×15	120	1.75	6×60.0	360.0	21, 41, 36, 30
UHW J245.32623−23.90277	2009 May 3	LowRes15	0.8×15	75	1.46	10×180.0	1800.0	22, 26, 19, 12
UHW J245.39963−23.91766	2008 Jul 2	LowRes15	0.5×15	120	1.43	11×30.0	330.0	147, 254, 231, 162
UHW J245.48320−23.35050	2012 Jul 6	LowRes15	0.3×15	200	1.54	9×15.0	135.0	147, 257, 279, 191
UHW J245.58499−23.13122	2009 May 3	LowRes15	0.5×15	120	1.73	8×180.0	1440.0	14, 33, 31, 34
UHW J245.66849−23.56412	2012 Jul 5	LowRes15	0.5×15	120	1.64	7×10.0	70.0	24, 63, 82, 63
UHW J245.68198−24.03424	2009 May 2	LowRes15	0.8×15	75	1.61	8×300.0	2400.0	20, 39, 33, 37
UHW J245.71139−24.22963	2009 May 6	LowRes15	0.8×15	75	1.41	8×180.0	1440.0	56, 67, 43, 37
UHW J245.81343−23.78480	2008 Jul 2	LowRes15	0.5×15	120	1.48	11×60.0	660.0	68, 156, 159, 142
UHW J245.87762−24.22221	2012 Jul 6	LowRes15	0.3×15	200	1.59	7×15.0	105.0	93, 183, 181, 136
UHW J245.95168−24.22649	2012 Jul 5	LowRes15	0.5×15	120	1.59	6×30.0	180.0	31, 85, 96, 63
UHW J246.06631−24.18753	2012 Jul 6	LowRes15	0.3×15	200	1.63	6×30.0	180.0	24, 63, 66, 45
UHW J246.51367−24.50719	2008 Jul 2	LowRes15	0.5×15	120	1.41	15×180.0	2700.0	4, 18, 28, 38
UHW J246.57742−24.49763	2008 Jul 2	LowRes15	0.5×15	120	1.48	10×180.0	1800.0	7, 41, 131, 225
UHW J246.62661−24.20326	2008 Jul 6	LowRes15	0.5×15	120	1.76	4×180.0	720.0	8, 55, 182, 306
UHW J246.65753−24.65089	2007 Jun 6	ShortXD	0.8×15	750	1.50	12×180.0	2160.0	17, 67, 109, 155
UHW J246.68094−24.17893	2008 Jul 3	LowRes15	0.5×15	120	1.85	10×60.0	600.0	174, 327, 292, 202
UHW J246.71774−24.02967	2008 Jun 27	LowRes15	0.5×15	120	1.45	7×180.0	1260.0	19, 54, 64, 71
UHW J246.73470−24.71048	2009 May 5	LowRes15	0.8×15	75	1.43	12×180.0	2160.0	16, 41, 36, 45
UHW J246.82722−24.12273	2008 Jul 3	LowRes15	0.5×15	120	1.45	10×60.0	600.0	82, 204, 239, 203

Table 5 continued on next page

Table 5 (*continued*)

Object	UT Date	Grat	Slit (")	R	sec z	$N_{\text{exp}} \times t$ (s)	T_{int} (s)	$\langle S/N \rangle$ (Y, J, H, K)
UHW J246.90062–24.08269	2007 Jun 7	ShortXD	0.8×15	750	1.39	12×90.0	1080.0	0, 48, 87, 132
UHW J246.92017–24.48353	2008 Jun 25	ShortXD	0.5×15	1200	1.47	10×300.0	3000.0	21, 61, 83, 106
UHW J246.94784–24.82865	2008 Jul 3	LowRes15	0.5×15	120	1.61	13×180.0	2340.0	34, 58, 51, 46
UHW J246.99312–23.98747	2008 Jul 2	LowRes15	0.5×15	120	1.59	10×30.0	300.0	93, 197, 204, 185
UHW J247.01994–24.84319	2008 Jun 27	LowRes15	0.5×15	120	1.42	10×15.0	150.0	40, 104, 105, 90
UHW J247.04356–24.40568	2007 Jun 5	LowRes15	0.5×15	120	1.47	8×180.0	1440.0	8, 41, 64, 106
UHW J247.19598–24.47051	2008 Jul 2	LowRes15	0.5×15	120	1.77	10×15.0	150.0	122, 211, 192, 153
UHW J247.20293–24.44216	2008 Jul 2	LowRes15	0.5×15	120	1.84	11×30.0	330.0	104, 189, 159, 123
UHW J247.20293–24.55216	2008 Jun 27	LowRes15	0.5×15	120	1.42	10×15.0	150.0	26, 53, 45, 34
UHW J247.38539–24.04299	2011 May 23	LowRes15	0.5×15	120	1.86	9×180.0	1620.0	17, 38, 31, 32
UHW J247.94088–24.62855	2007 Jun 7	ShortXD	0.8×15	750	1.44	12×60.0	720.0	25, 96, 151, 214
UHW J247.95427–24.78060	2011 May 23	LowRes15	0.5×15	120	1.53	12×180.0	2160.0	10, 29, 23, 30
UHW J248.69073–24.82275	2008 Jul 2	LowRes15	0.5×15	120	1.56	11×180.0	1980.0	70, 99, 79, 52

NOTE—The last column gives the median S/N of the spectrum within the standard IR bandpasses.

Table 6. Classification of Candidate Members

Object	SpT	A_V	Gravity	Lit SpT	Lit Ref	DR2 plx	DR2 pmra	DR2 pmdec
NGC 1333						3.38±0.32	7.34±0.92	-9.90±0.6
UHW J052.25592+30.82075	M7	0.00±0.40	VL-G			3.68±0.23	6.72±0.30	-11.22±0.25
UHW J052.26618+30.94156			12.62±1.95	11.90±2.32	-3.36±1.84
UHW J052.27886+31.49911	M8	4.63±0.76	VL-G	M7, M7-M9	S12, L16			
UHW J052.30643+31.39637					
UHW J052.35191+31.47077	M6	3.33±0.64	VL-G	M7.4, M7, M5	W04, S12, L16	3.63±0.35	6.00±0.57	-9.06±0.37
UHW J052.40147+31.29717	L0	0.00±1.69	VL-G	late-M, M9	S09, L16			
UHW J052.43392+31.32982	M8	5.66±2.13 ^a	VL-G	~M9, M6-M8.5	S12, L16			
UHW J052.75599+30.63090	L0	0.00±1.32	VL-G					
IC 348						3.09±0.26	4.35±0.24	-6.76±0.52
UHW J055.48646+31.83838	M5	0.92±0.46	...			7.08±0.38	-24.69±0.53	-6.45±0.33
UHW J055.54657+31.94999			1.52±1.74	0.83±2.88	-2.55±1.77
UHW J055.55875+31.95973			0.29±0.60	1.22±0.90	-1.82±0.55
UHW J055.67611+31.72142	M8	5.85±1.17	INT-G					
UHW J055.71237+31.94127	M7	2.54±1.17	INT-G					
UHW J055.73277+32.07455	M7	1.23±1.15	VL-G			4.47±0.66	3.96±1.15	-6.30±0.67
UHW J055.75603+32.03731	M6	2.73±0.64	VL-G	M5.25	L16	3.58±0.43	5.70±0.87	-7.67±0.57
UHW J055.75810+31.74320	M7	4.55±0.54	VL-G			2.85±1.05	1.39±1.32	-9.35±1.00
UHW J055.76964+32.16007	M8	3.97±1.17	VL-G					
UHW J055.98976+32.24691	M7	1.17±0.54	VL-G	M6	L16	2.22±0.61	4.07±1.18	-6.41±0.6
UHW J056.01221+31.87436	M6	4.68±0.64	VL-G	M6	L16	3.19±0.81	4.59±1.28	-6.37±0.83
UHW J056.04265+31.54385	M8	0.94±1.01	VL-G					
UHW J056.07487+31.58792					
UHW J056.14403+31.71225	M6	5.94±0.51	VL-G			5.11±1.29	4.65±2.31	-7.30±1.48
UHW J056.17321+32.17758	M6	1.98±0.51	VL-G	M5.75	L98	4.37±0.84	4.43±1.44	-6.68±0.86
UHW J056.34957+32.19849	M7	2.51±0.54	VL-G	M5.75, M6.5	A13, L16	3.92±0.96	2.57±1.62	-7.20±1.18
UHW J056.37556+31.62740					
UHW J056.38941+31.76537	M6	7.92±0.51	VL-G			3.06±1.66	8.00±3.41	-2.85±1.81
Ophiuchus						7.1±0.4	-7.2±2.0	-25.5±1.7
UHW J245.25929-23.97766	M6	3.86±0.51	INT-G	M5.25	L12	7.43±0.57	-13.11±1.18	-25.30±0.77
UHW J245.32623-23.90277					
UHW J245.39963-23.91766	M6	2.02±0.64	VL-G	M6	S06	7.42±0.28	-12.31±0.57	-24.36±0.37
UHW J245.48320-23.35050			7.14±0.14	-11.23±0.29	-24.28±0.17
UHW J245.58499-23.13122	L0	2.11±2.07	VL-G					
UHW J245.66849-23.56412			7.19±0.22	-9.61±0.48	-25.75±0.3
UHW J245.68198-24.03424	M7	5.29±0.41	VL-G					
UHW J245.71140-24.22963	M5	0.63±0.31	...			7.63±0.40	-20.18±0.77	-27.58±0.55
UHW J245.81343-23.78480	M8	3.98±1.17	VL-G			7.86±1.28	-0.77±3.41	-23.96±2.19
UHW J245.87762-24.22221	M6	3.14±0.64	VL-G			6.80±0.17	-7.47±0.31	-24.66±0.19
UHW J245.95168-24.22649	M7	6.70±1.27	VL-G			4.96±0.50	-5.65±0.89	-33.75±0.61
UHW J246.06631-24.18753	M6	5.99±0.51	VL-G			6.57±0.36	-6.13±0.79	-23.60±0.53
UHW J246.51367-24.50719	L1	4.56±4.40	VL-G	L0, M9.7	A12, M12			
UHW J246.57742-24.49763	M9	13.21±3.18	VL-G	M6.75, M8.6	A12, M12			
UHW J246.62662-24.20326	M6	19.84±1.27	VL-G					
UHW J246.65753-24.65089	M6	7.79±0.51	VL-G	M5.25, M6.4	A12, M12	7.07±1.07	-7.59±2.40	-25.48±1.77

Table 6 continued on next page

Table 6 (*continued*)

Object	SpT	A_V	Gravity	Lit SpT	Lit Ref	DR2 plx	DR2 pmra	DR2 pmdec
UHW J246.68094–24.17893	M6	4.07±0.51	VL-G			7.66±0.27	-10.00±0.55	-27.03±0.35
UHW J246.71774–24.02967	M7	7.32±1.17	VL-G	M7.5	A10			
UHW J246.73470–24.71048	L0	1.83±1.87	VL-G	M9	G11			
UHW J246.82722–24.12273	M6	7.38±0.51	INT-G	M7.5	A12	6.76±1.29	-3.80±3.24	-27.21±1.78
UHW J246.90062–24.08269	M6	8.22±0.51	VL-G			6.43±0.65	-9.02±1.42	-23.89±0.84
UHW J246.92017–24.48353	M9	2.49±1.96	VL-G	M7.75, M8.2	A12, M12	7.14±0.70	-9.46±1.42	-25.99±0.96
UHW J246.94785–24.82865					
UHW J246.99312–23.98747	M8	2.93±1.17	VL-G			5.46±0.60	-6.83±1.18	-25.08±0.76
UHW J247.01994–24.84319	M6	5.35±0.76	INT-G			5.99±0.41	-6.59±0.88	-25.22±0.65
UHW J247.04356–24.40568	L0	7.51±2.07	VL-G	L0	A12			
UHW J247.19598–24.47051	M6	3.19±0.64	VL-G	M6	S08	7.12±0.20	-9.52±0.39	-26.44±0.26
UHW J247.20293–24.44216	M7	1.60±1.17	VL-G	M6.25	A12	6.26±0.50	-3.93±0.88	-26.74±0.61
UHW J247.20293–24.55216	M7	0.89±0.96	VL-G					
UHW J247.38539–24.04299	M6	6.42±0.41	FLD-G					
UHW J247.94088–24.62855	M8	5.38±2.37	VL-G					
UHW J247.95427–24.78060	L1	0.00±1.25	VL-G					
UHW J248.69073–24.82275			-0.33±0.38	1.02±0.74	-3.50±0.51

NOTE—Mean and standard deviation for Gaia DR2 parallaxes and proper motions are from [Ortiz-León et al. \(2018\)](#) for IC 348 and NGC 1333 and [Cánovas et al. \(2019\)](#) for Ophiuchus.

^aReddening determined from $J - H$ color rather than $J - K$, as K -band flux is anomalously high relative to J and H . [Luhman et al. \(2016\)](#) interpret this as being scattered light from an edge-on disk.

References— A10: [Alves de Oliveira et al. \(2010\)](#); A12: [Alves de Oliveira et al. \(2012\)](#); A13: [Alves de Oliveira et al. \(2013\)](#); G11: [Geers et al. \(2011\)](#); L98: [Luhman et al. \(1998\)](#); L12: [Luhman, & Mamajek \(2012\)](#); L16: [Luhman et al. \(2016\)](#); M12: [Mužić et al. \(2012\)](#); S06: [Slesnick et al. \(2006\)](#); S08: [Slesnick et al. \(2008\)](#); S09: [Scholz et al. \(2009\)](#); S12: [Scholz et al. \(2012\)](#); W04: [Wilking et al. \(2004\)](#)